This article has been accepted for publication in a future issue of this journal, but has not been fully edited. Content may change prior to final publication. Citation information: DOI 10.1109/TTE.2022.3175806, IEEE Transactions on Transportation Electrification

Multi-Objective Thermal Optimization Based on Improved Analytical Thermal Models of a 30 kW IPT System for EVs

Baokun Zhang, *Student Member, IEEE*, Junjun Deng, *Member, IEEE*, Wenbo Wang, *Student Member, IEEE*, Lantian Li, *Student Member, IEEE,* Zhenpo Wang, *Senior Member, IEEE,* Shuo Wang, *Member, IEEE,* and Giuseppe Guidi, *Senior Member, IEEE*

***Abstract*—Thermal design is particularly important for high-power and compact inductive power transfer (IPT) systems having limited surface area for heat dissipation. This paper presents the thermal design and optimization of a 30 kW IPT system for electric vehicles. An improved analytical thermal model with high accuracy for liquid-cooled magnetic couplers was proposed by using thermal network method (TNM). It considers heating components as well as thermal interface materials. Then multi-objective thermal optimization procedure of the liquid-cooled magnetic coupler was conducted with the presented model. Tradeoffs among temperature rise, weight, and cost were discussed and an optimized solution was selected. The thermal FE models were established and compared with the thermal networks. Subsequently, the thermal performance of the system at different power levels and misaligned conditions was analyzed. The experimental setup based on Fiber Bragg grating sensors was built, and the prototypes were tested with an output power of around 28 kW. The error of stable temperature between the experiment and the prediction was less than 10% at the measurement points, verifying the thermal models. The proposed thermal models and optimization procedure accelerate the thermal design of IPT systems, towards higher power density.**

***Index Terms*—Inductive power transfer, Thermal analysis, Thermal network method, Pareto optimization, Wireless charger.**

I. Introduction

Inductive power transfer (IPT) technique allows power to be transferred between two systems by magnetic coupling without electrical contacts. With the advantages of convenience, safety, and low maintenance cost, IPT is getting increasing applications, especially the wireless charging of electric vehicles (EVs) [1]. Recent broad applications of wireless chargers to electrified transportation have indicated a trend toward higher power and power density of designs [2]. The induced eddy current losses in magnetic components have a detrimental effect on the performance and reliability of chargers [3]. In low-power applications, the thermal design of IPT systems does not require much extra attention because the limited heat dissipation can be easily removed by air cooling. However, for high-power IPT systems with limited surface area and compact packing, heat dissipation cannot be ignored, necessitating increased concern in the thermal design and optimization of IPT systems. The relevant methods and studies in recent years are summarized below.

Thermal network method (TNM) is an analytical solution to calculate the thermal behavior via thermal resistor networks. It's computationally quick and straightforward, but the accuracy is limited for systems with non-linear material properties and complex shapes. Meanwhile, finite element method (FEM) is another mainstream method. It takes longer to calculate but is more accurate and allows to view the temperature distribution. On this basis, computational fluid dynamics (CFD) extends the thermal (and perhaps electromagnetic) FEM, replacing the simple boundary conditions of convective heat transfer with an explicit modeling of the heat transfer process at the wall.

The thermal networks of a transformer composed of windings and magnetic cores can be found in [4] – [6]. In [7], the thermal equivalent circuit of the winding, cores, thermally conductive plastic plates, and aluminum plates is modeled, considering the thermal resistance and heat capacity of the materials. In [8] – [10], simplified thermal networks have been established for the 50 kW rectangular coil, ferrite I-core, as well as capacitors and heatsinks, respectively. On this basis, the maximum surface-related power loss density is viewed as the thermal limit, and the finite element (FE) tool is used to validate the thermal feasibility of the coil design. In [11] – [12], the thermal analysis of a magnetic coupler is conducted by FE

This work was supported by the National Key Research and Development Program of China (No. 2019YFE0104700). (*Corresponding author: Junjun Deng*).

Baokun Zhang, Junjun Deng, Wenbo Wang, Lantian Li, Zhenpo Wang, and Shuo Wang are with the National Engineering Research Center of Electric Vehicles, School of Mechanical Engineering, Beijing Institute of Technology, No. 5 Zhongguancun Street, Haidian District, Beijing 100081, China (e-mail: bk.zhang@foxmail.com; dengjunjun@bit.edu.cn; wenbo@bit.edu.cn; ericlee0126@gmail.com; wangzhenpo@bit.edu.cn; shuo.wang@bit.edu.cn).

Giuseppe Guidi is with the Electric Power System Department, SINTEF Energy Research, Sem Sælands vei 117034 Trondheim (e-mail: Giuseppe.Guidi@sintef.no).

2332-7782 (c) 2021 IEEE. Personal use is permitted, but republication/redistribution requires IEEE permission. See http://www.ieee.org/publications_standards/publications/rights/index.html for more information.
Authorized licensed use limited to: Sintef. Downloaded on May 20,2022 at 10:23:19 UTC from IEEE Xplore. Restrictions apply.

This article has been accepted for publication in a future issue of this journal, but has not been fully edited. Content may change prior to final publication. Citation information: DOI 10.1109/TTE.2022.3175806, IEEE Transactions on Transportation Electrification

softwares. The thermal resistance model of a receiver is established from a qualitative point of view, and the temperature distribution of each component is studied with FE simulations [13]. The sensitivity of ground assembly (GA) surface temperature to different misalignments [14] of a commercialized wireless charging system is analyzed based on FEM. In [15], the proposed thermal simulation model for vehicle assembly (VA) structures is verified, which uses analytically calculated power losses and considers the temperature dependence. In [16], thermal analysis based on FEA of a 50 kW three-phase wireless charging system is presented.

Other studies have focused on the coupling between thermal and electromagnetic fields. A co-simulation method is proposed in [17], where the electromagnetic part is simulated in the frequency domain while the thermal part remains in the time domain. Similarly, the frequency-transient multiphysics analysis is presented in [18]. Alsayegh developed a combined electromagnetic-thermal reduced order model [19], and the relationship between temperatures and losses over time can be obtained by coupling the magnetic and thermal field solvers. A similar study using magneto-thermal simulation for three types of coil structures is performed in [20]. Kim conducted a numerical thermal analysis of a double-D buried primary pad within a model pavement and proposed a flow diagram of iterative two-way coupled electromagnetic-thermal FE simulations of the pad and pavement performance [21] - [22]. In [23], for simplification of simulations, the CFD simulation is not carried out to model the flow of air around the pad. Instead, the average convection coefficients are calculated and applied to the surfaces exposed to air. A fully coupled numerical method for the analysis of the wireless power transfer system is presented in [24]. With the two-way integration of the CFD and electromagnetic FEM, the effect of electromagnetic and ohmic losses on the thermal performance of the IPT system is investigated. Furthermore, Moghaddami investigated a multiphysics model in [25]. It combines electromagnetic, thermal, and fluid dynamics models incorporating the air convection process and therefore results in more accurate thermal performance analysis.

The literature mentioned above has made beneficial explorations in establishing thermal models, studying the thermal performance of the system, predicting the temperature with time, etc. Multiphysics coupling based on the numerical calculation method is a development trend. The two-way coupling solution of the thermal field and the electromagnetic field, even coupled with the fluid field, improves the accuracy of the simulation. However, it is computationally expensive during optimization, and designers have little freedom to automate the optimization process [26]. On the other hand, calculation and optimization by the TNM-based thermal model have the advantage of being efficient and time-saving, which is more suitable for thermal design in this regard. Therefore, analytical thermal models with appropriate complexity and accuracy are required for magnetic couplers. The thermal optimization process and method for IPT couplers are necessary, too.

A search of the literature revealed that few studies focus on the analytical thermal models or the thermal optimization process and method for IPT systems. The thermal model of transformers whose cores and windings are axially symmetric is presented in [4-6]. The simplified thermal models for I-type cores, planar windings, and capacitors can be found in [8-10]. They are used to eliminate thermal designs that exceed the estimated thermal limit in the optimization procedure of IPT coils, and the accuracy needs to be improved. The above one-dimensional thermal models, i.e., thermal resistances are in series, show validity with the symmetrical structure and simple application scenarios (heating components - (heatsinks) - cooling fluids). However, for the system with slightly complicated structures and heat dissipation conditions, the simplified models need to be improved for the following reasons.

1) Considering the contact of heating components in magnetic couplers, it is better to establish the winding, cores, and aluminum shielding in the same thermal model, taking their power loss into account.

2) Previous studies have not dealt with the thermal interface materials between heating components in IPT systems. In practice, their thermal resistance should be included in thermal networks, and the effect of each thermal resistance on the temperature rise must be quantified.

3) The heat dissipation path at different positions of the same heating component may be different and the one-dimensional thermal resistance model cannot accurately describe the differences. Therefore, it is required to expand the model into a two-dimensional or even three-dimensional multipath thermal resistance network. Whereas, if the thermal network is too complex, the choice between TNM and FEM requires discussion.

To supplement the above deficiencies, improved analytical thermal models are proposed for the magnetic coupler of IPT systems. The established two-dimensional thermal networks consist of multiple heat transfer paths from heat sources to the ambient, which consider the main factors affecting heat conduction and heat dissipation, such as potting compounds, thermal interface materials, and fluid state. In addition, the thermal resistances are quantified to calculate the average temperature of the heating components. Compared to previous works, the proposed thermal network allows for inclusion of more detailed models, thus yielding more accurate results while retaining relatively low computational complexity. The method is therefore suited for implementation of iterative thermal design and optimization algorithms for IPT systems.

Besides, a multi-objective thermal optimization procedure based on Pareto front for magnetic coupler is proposed. It takes the temperature rise, weight, and cost into account. This work helps to achieve higher power density and lighter weight for IPT systems.

This is an enhanced version of the paper presented in [27] with a more detailed thermal design process and experimental results. Specifically, 1) a multi-objective thermal optimization

2332-7782 (c) 2021 IEEE. Personal use is permitted, but republication/redistribution requires IEEE permission. See http://www.ieee.org/publications_standards/publications/rights/index.html for more information.
Authorized licensed use limited to: Sintef. Downloaded on May 20,2022 at 10:23:19 UTC from IEEE Xplore. Restrictions apply.

This article has been accepted for publication in a future issue of this journal, but has not been fully edited. Content may change prior to final publication. Citation information: DOI 10.1109/TTE.2022.3175806, IEEE Transactions on Transportation Electrification

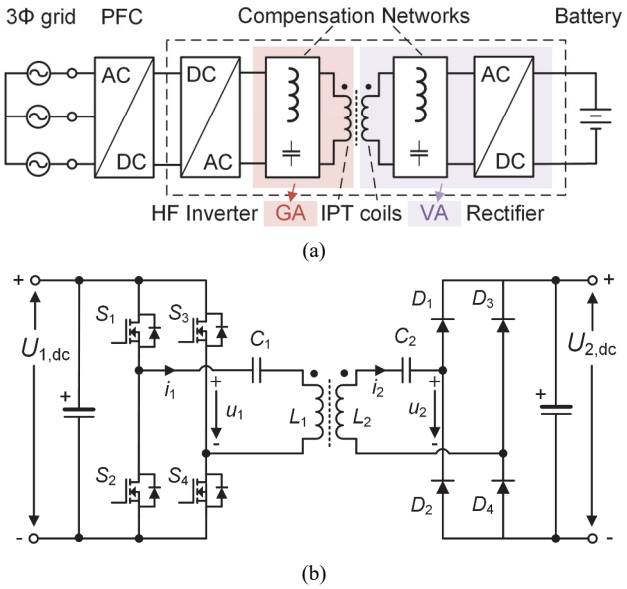

Fig. 1. (a) Block diagram of the IPT system (b) Specific circuit in the dashed frame.

procedure of magnetic couplers for EVs is proposed; 2) the thermal analysis and design of the naturally cooled GA are included; 3) the maximum cooling capacity and thermal limit of the realized prototype are explored, and the influence of different power levels and misalignments on the temperature rise is analyzed; 4) the scope of application and features of TNM and FEM are discussed. The remaining part of this paper proceeds as follows: Section II describes the IPT system; in Section III, improved thermal models are proposed using TNM; in Section IV, the multi-objective thermal optimization procedure is presented; in Section V, the thermal performance of the system is studied; experimental verification is shown in Section VI; finally, the work is concluded in Section VII.

II. The IPT System

The objective of this paper is to design a 30 kW IPT system for electric vehicle applications. All devices on the receiver side need to be integrated into VA and then installed under the chassis, while the magnetic components and compensation capacitors at the transmitter side are required to be integrated into GA, and the upper surface of GA is kept flush with the ground. The system should have maximum power output capability at both aligned and misaligned positions, and the system must be thermally feasible under these conditions.

The air gap, operating frequency, and other specifications for the system are listed in Table I. The block diagram of this

TABLE I
Specification of The IPT System

Variable	Value	Description
P_{max}	30 kW	Maximum output power
δ	170 mm	Rated air gap
f	85 kHz	Operating frequency
$U_{1,dc}$	250~650 V	Transmitter-side dc-link voltage
U_{batt}	360~550 V	Battery voltage

TABLE II
Design Values of the IPT System

Variable	Value	Description
L_1&L_2	75.1 μH	Self-inductance
M	13.4 μH	Mutual inductance
C_1&C_2	46.7 nF	Compensation capacitance
l_{coil}	440×380 mm	Coil size (L×W)
l_{core}	540×390 mm	Core size (L×W)

TABLE III
The Used Material and Product Model

Material/Device	Type	Description
Litz wire	Silk-covered wire	0.1 mm×2500
Ferrite core	DMR 95, I type	15 mm-thick
Compensation capacitor	CSP 120/200	0.33 μF×7
MOSFET	SiC half-bridge module	CAS120M12BM2
Rectifier diode	SiC schottky diode	C4D40120D

IPT system is shown in Fig. 1(a). An ac–dc converter with power factor correction (PFC) for the grid current is used to produce a controllable dc-link voltage. The IPT system consists of a high-frequency (HF) inverter on the transmitter side, resonant compensation networks for the coils, and a rectifier circuit on the receiver side. The specific circuit structure in the dashed frame is shown in Fig. 1(b).

Series-series (SS) compensation topology is selected. L_1 and L_2 are the self-inductance of the transmitting and receiving coils, respectively. C_1 and C_2 are the transmitter side and receiver side compensation capacitors, respectively. Identical windings, ferrite cores, and compensation capacitors on the transmitter and receiver side are used for simplicity. Their design values are shown in Table II. S_1~S_4 are four power MOSFETs on the transmitter side. D_1~D_4 are the receiver side rectifier diodes. The used materials and devices are summarized in Table III.

Neglecting the losses in the system, the transmitted power follows [8] as

$$P_2 \approx \frac{8}{\pi^2}\frac{U_{1,dc}U_{2,dc}}{\omega M} \tag{1}$$

where $U_{1,dc}$ and $U_{2,dc}$ are the dc-link voltage of transmitter side and receiver side, respectively. ω is the resonant angular frequency and M is the mutual inductance of the IPT coils.

The fundamental harmonic approximation (FHA) is applied under static-state conditions. u_1, u_2 are both rectangular voltages while i_1 and i_2 are sine wave currents due to the filtering effect of the resonant network. The fundamental frequency components of u_1 and u_2 are $U_{1(1)}$ and $U_{2(1)}$, respectively, while I_1 and I_2 represent RMS current of i_1 and i_2.

By Kirchhoff's law, it is easy to attain

$$\begin{aligned} U_{1(1)} &= -j\omega M I_2 + j\omega L_1 I_1 + \frac{I_1}{j\omega C_1} \\ U_{2(1)} &= j\omega M I_1 - j\omega L_2 I_2 - \frac{I_2}{j\omega C_2} \\ \hat{U}_{2(1)} &= \frac{4}{\pi}U_{2,dc} \end{aligned} \tag{2}$$

2332-7782 (c) 2021 IEEE. Personal use is permitted, but republication/redistribution requires IEEE permission. See http://www.ieee.org/publications_standards/publications/rights/index.html for more information.
Authorized licensed use limited to: Sintef. Downloaded on May 20,2022 at 10:23:19 UTC from IEEE Xplore. Restrictions apply.

This article has been accepted for publication in a future issue of this journal, but has not been fully edited. Content may change prior to final publication. Citation information: DOI 10.1109/TTE.2022.3175806, IEEE Transactions on Transportation Electrification

$\hat{U}_{2(1)}$ is the peak value of fundamental voltage $U_{2(1)}$

$$U_{2(1)} = \frac{1}{\sqrt{2}} \hat{U}_{2(1)} \tag{3}$$

The capacitance values are given by

$$C_1 = \frac{1}{\omega^2 L_1} \quad C_2 = \frac{1}{\omega^2 L_2} \tag{4}$$

Substituting (3) and (4) into (2), we can get the current of the transmitter side

$$I_1 = \frac{2\sqrt{2}}{\pi} \frac{U_{2,dc}}{\omega M} \tag{5}$$

For constant-voltage output and fixed-frequency applications, the current in the transmitting coil increases to maintain the rated output power when the mutual inductance decreases. The effect of coil misalignment will be discussed in Part B of Section V.

III. Improved Analytical Thermal Models Based on TNM

The general assumption of TNM is described as follows. The real heat sources and thermal resistances are replaced by a few lumped heat sources and equivalent thermal resistances, and the temperature field is transformed into a thermal resistance network for calculation. Heat transfer from hotspots to the ambient environment takes several different paths, and each path is composed of series and or parallel thermal resistances. When power losses are applied to the nodes of two-dimensional thermal networks in the form of point heat sources, the temperature rise can be calculated. It is easy to understand that the principle of thermal design is to provide heat transfer paths whose thermal resistance is as low as possible.

In this section, the cooling method is selected for VA and GA, respectively. And an integrated design is proposed according to the demand of the system. Then, the calculation formulas for power loss and the related theory of heat transfer are briefly introduced. After that, the thermal analysis of heating components is conducted with the improved thermal networks.

A. Cooling Method Selection and Components Layout

The cooling methods are chosen first. For VA, forced air cooling is not adopted because the rotating parts of cooling fans are prone to wear, which could affect the reliability of VA. Besides, it has previously been observed that the charging power of IPT systems with natural convection cooling is limited to 3-5 kW [28]. The installation of additional heatsinks facilitates the effect of natural cooling, but it increases the overall height of VA, easily exceeding the size limit. Instead, if conditions permit, liquid cooling is preferable to utilize the limited space under the vehicle chassis. For GA, due to the large space available, we choose natural cooling with heatsinks installed under the shell of GA.

Next, an integrated design scheme of magnetic coupling coils and power conversion components is proposed. All components of VA are mechanically integrated inside the enclosure. Fig. 2(a) shows the layout within VA. The winding and ferrite cores

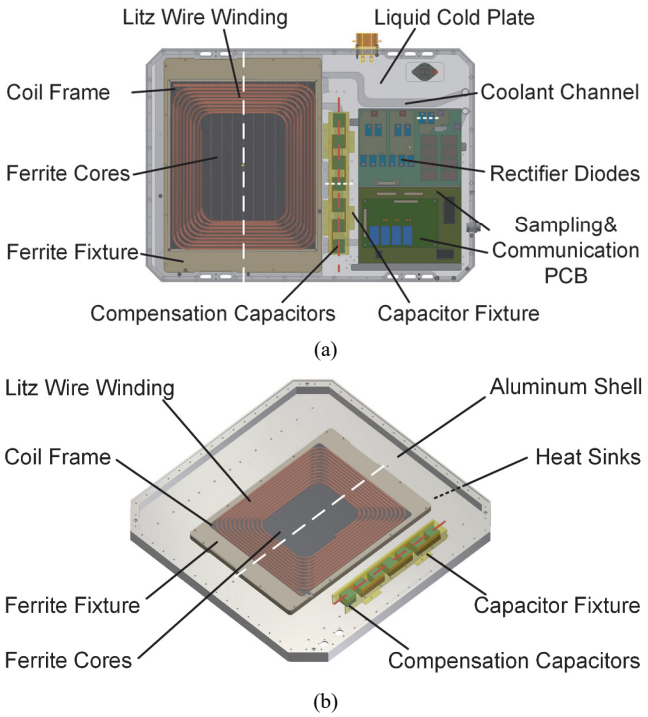

Fig. 2. The proposed integrated layout of inner components in (a) VA and (b) GA.

are closely attached to improve the magnetic property by a coil frame. The ferrite cores are installed on the liquid cold plate by the ferrite fixture. The compensation capacitors are fixed on the cold plate by a dedicated fixture. The rectifier diodes are mounted on the aluminum plate and then attached to the cold plate. The coolant channel is distributed evenly inside the liquid cold plate according to the layout of these components. The PCB is used for output current sampling, circuit protection on the receiver side, and communication with the GA and EV. Finally, the enclosure is sealed with a plastic cover to avoid environmental contamination. For the transmitter side, no additional components except the winding, cores, and capacitors are integrated into GA. PFC and HF inverter are installed in an additional box and equipment cabinet, respectively. Four heat sinks are installed side by side under the aluminum shell of GA. And the inner arrangement is similar to that of VA, as shown in Fig. 2(b).

B. Power Loss Analysis

System power losses consist of: (a) magnetic coupling components (Litz wire, ferrite cores, and aluminum shielding), (b) compensation capacitors, and (c) power electronics devices (MOSFET, diode) [29]. As the heat inputs of thermal models, they are briefly discussed as follows.

For the IPT coils, the ac-to-dc resistance ratio $k_{\mathrm{ac-dc}}$ is used to describe the total losses of the winding when the system is operated at a certain frequency. The winding copper loss can be calculated by

$$P_{winding} = I_{rms}^2 R_{dc} \cdot k_{ac-dc} \tag{6}$$

where R_{dc} and $k_{\mathrm{ac-dc}}$ can be estimated according to the design

2332-7782 (c) 2021 IEEE. Personal use is permitted, but republication/redistribution requires IEEE permission. See http://www.ieee.org/publications_standards/publications/rights/index.html for more information.
Authorized licensed use limited to: Sintef. Downloaded on May 20,2022 at 10:23:19 UTC from IEEE Xplore. Restrictions apply.

This article has been accepted for publication in a future issue of this journal, but has not been fully edited. Content may change prior to final publication. Citation information: DOI 10.1109/TTE.2022.3175806, IEEE Transactions on Transportation Electrification

manual [30] and the modeling approach presented in [9]. I_{rms} is the RMS value of the current in the winding.

The power loss of the ferrite cores can be calculated by integrating the core loss density p_{core} over the volume of cores. The loss density is evaluated from the flux density obtained with electromagnetic FE simulation and the standard Steinmetz equation:

$$P_{core} = C_m f^{\alpha} \hat{B}^{\beta} \tag{7}$$

where $\hat{B}$ is the peak magnetic flux density. C_{m}, α, and β are three coefficients of the ferrite material, which are typically provided by the manufacturer.

Similarly, the eddy current losses P_{al} on aluminum shells are obtained from FE tools.

For polypropylene film capacitors of type CSP 120/200, due to their voltage rating, a series connection of seven devices is required through copper busbars. Dissipation factor $\tan\delta$ is a key parameter in modeling the capacitor losses, and its value is around 1.4×10^{-3} at the selected frequency [9].

$$P_{cap} = \tan\delta \cdot I_{rms}^2 \big/ 2\pi f C \tag{8}$$

The losses of power electronic devices on the receiver side are mainly caused by the rectifier. The switching and conduction losses are calculated according to the datasheet and equations presented in [31].

C. Fundamentals of Heat Transfer

The heat transfer mechanisms are conduction, convection, and radiation. Radiation has little effect on the temperature rise of this IPT system. In addition, the thermal resistance representing radiation is nonlinear, which complicates the calculation. Therefore, only conduction and convection are considered. The steady-state temperature of the system is the main concern in the thermal design, thus the thermal behavior can be characterized simply by an equivalent thermal resistance R_{th}. Formulas for determining the resistance are given below.

In the mechanism of conduction, for a cube with conduction length L_c , cross-section A, and thermal conductivity k, its thermal resistance inside the material can be calculated by

$$R_{th\_cd} = L_c \big/ kA \tag{9}$$

Note that the concept of thermal resistance cannot be applied directly to materials where there is internal heat generation (like the windings or the cores). This is particularly true if the heat generation is not uniform. Besides, the effective cross-sectional area of heat conduction is not equal to the cross-sectional area of the material. For the case where heat passes through two materials in turn, if their cross-sectional area and thermal conductivity are different, it is recommended to multiply by an area correlation coefficient during calculation.

In the mechanism of convection, the thermal resistance between the surface and the ambient can be calculated by

$$R_{th\_cv} = 1 \big/ h_{conv} A_{surf} \tag{10}$$

where A_{surf} is the area of the exposed surface, and h_{conv} is the convection coefficient. The empirical formulas for the convection coefficient of fluid are introduced below.

For a rectangular channel with the width w and height h, its hydraulic diameter and geometric parameter (G) follow

$$d_h = 2wh / (w + h) \tag{11}$$

$$G = \left[\left(\frac{w}{h} \right)^2 + 1 \right] \Big/ \left(\frac{w}{h} + 1 \right)^2 \tag{12}$$

If the Reynolds number (Re) is less than 2300, the fluid flow is laminar and the expressions of Nusselt number Nu and friction factor f are given by [32]

$$Nu = -1.047 + 9.326G \tag{13}$$

$$f = (4.7 + 19.64G) \big/ \mathrm{Re} \tag{14}$$

If the Reynolds number is equal to or higher than 2300, the Nusselt and friction factor become

$$Nu = \frac{\frac{f}{2}[\mathrm{Re} - 100]\mathrm{Pr}}{1 + 12.7\sqrt{\frac{f}{2}}\left(\mathrm{Pr}^{\frac{2}{3}} - 1\right)} \tag{15}$$

$$f = \left(0.0929 + \frac{1.01612 d_h}{L}\right) \mathrm{Re}^{(-0.268 - (0.3193 d_h / L))} \tag{16}$$

where Pr is the Prandtl number and L is the length of the channel.

For the flow in serpentine-channel, due to the existence of bent pipes which can break fluid thermal boundary layer, using (13)-(16) to calculate h_{conv} is not precise [33]. Therefore, the average Nusselt number Nu_m is introduced to calculate h_{conv_m}. The empirical formula of Nu_m is as follows [34]:

$$Nu_m = \left\{ \left[2.22 \left(x^* \right)^{-0.33} \right]^3 + Nu^3 \right\}^{1/3} \tag{17}$$

where x^* is a dimensionless number representing the thermal entrance length, $x^* = L/(Re d_h Pr)$.

Then the average convection coefficient between the coolant channel and the fluid can be obtained by:

$$h_{conv\_m} = Nu_m k_f \big/ d_h \tag{18}$$

where k_f is the thermal conductivity of the fluid.

The serpentine channel can be thought of as a combination of straight pipes and bent pipes, and its total pressure loss consists of friction loss of all pipes and excess loss of bent pipes. To simplify the calculation and avoid time-consuming CFD simulations, the total pressure drop is estimated according to the following equation[32].

$$\Delta p = 4 f \rho \frac{L_{eq}}{d_h} \frac{v^2}{2} \tag{19}$$

$$L_{eq} = \sum l_{straight} + \sum l_{bent} \tag{20}$$

ρ and v are the density and velocity of the fluid, respectively. L_{eq} is defined as the equivalent total length of the channel. It is the sum of the length of straight pipes and the equivalent length of bent pipes. Allowing for friction loss and excess loss, the equivalent length of bent pipe is considered to be several times the hydraulic diameter of the channel. r is the radius of bent pipe.

$$l_{bent} = d_h \cdot 73.83 / \left(r \big/ d_h + 1.22 \right) \tag{21}$$

D. Thermal Modeling of Heating Components Based on TNM

To simplify the thermal model, three assumptions are made. First, the thermal contact resistance is ignored and the surfaces of the components fit together as closely as possible by adding

2332-7782 (c) 2021 IEEE. Personal use is permitted, but republication/redistribution requires IEEE permission. See http://www.ieee.org/publications_standards/publications/rights/index.html for more information.
Authorized licensed use limited to: Sintef. Downloaded on May 20,2022 at 10:23:19 UTC from IEEE Xplore. Restrictions apply.

This article has been accepted for publication in a future issue of this journal, but has not been fully edited. Content may change prior to final publication. Citation information: DOI 10.1109/TTE.2022.3175806, IEEE Transactions on Transportation Electrification

thermal interface materials and applying an external force. Second, the temperature-dependent characteristic parameters (like thermal conductivity and resistivity) at the expected final approximate temperature are adopted. Third, thermal cross-coupling effects are not considered, meaning that the different heating components in the model are considered basically independent. The key materials and their thermal property parameters are summarized in Table IV. The material of coil frames and ferrite fixtures is acrylonitrile-butadiene-styrene (ABS), while that of capacitor fixtures is polycarbonate (PC) and its thermal limit is higher.

TABLE IV
THERMAL PROPERTIES OF KEY MATERIALS

Material	Thermal Conductivity (W/m·K)	Thermal Limit (°C)
Ferrite core	4	120
Litz wire	1 [35]	120
Metallized film dielectric	43.6 [36]	90
Diode	R_{jc}=0.31(K/W)	175
Acrylonitrile-butadiene-styrene (ABS)	0.25	80
Polycarbonate (PC)	0.2	120

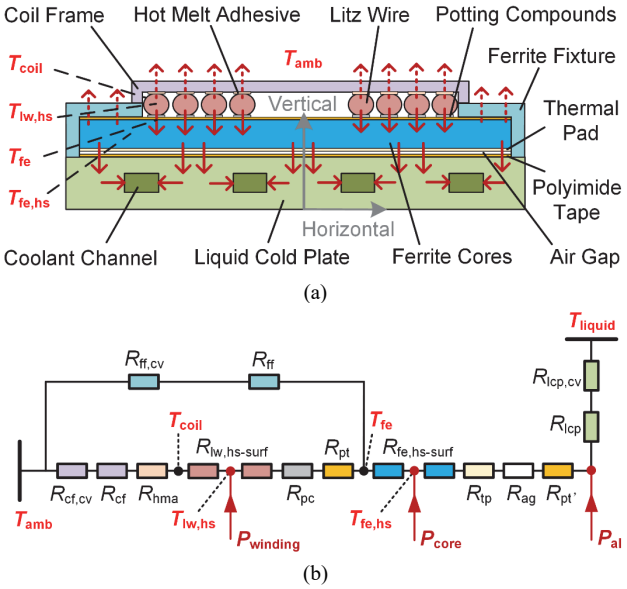

Fig. 3. Thermal analysis and modeling of the winding and cores in VA. (a) heat transfer path and (b) thermal network.

1) *Litz Wire Winding and Ferrite Cores of VA*

The Litz wire winding is adhered to the coil frame with a thin layer of hot melt adhesive, with potting compounds on the other side attached to the ferrite cores. Because the VA is mounted upside down, there will be a tiny air gap between the ferrite cores and the liquid cold plate under the action of gravity. This gap has a great effect on the temperature rise, which should be avoided by applying a layer of thermal grease. It is also an ideal place for corona discharge to happen and may cause insulation failures. Besides, the insulation in some positions may fail due to mechanical wear and tear. Therefore, polyimide tape is used additionally in the VA for electrical insulation at high temperatures for safety's sake.

Assume that temperature hotspots are homogeneous and located in the central plane of the winding and cores, respectively ($T_{\mathrm{lw,hs}}$ and $T_{\mathrm{fe,hs}}$). Since the material is symmetric about the central plane, equal models are assumed for the top and bottom winding surfaces. For the ferrite cores, an analogous model is used. In this case, the top and bottom surfaces of the winding and ferrite cores are considered. The horizontal heat transfer path is not considered for two main reasons: first, the temperature difference within the component is not significant because of relatively high thermal conductivity, generally only a few degrees; second, the side heat conduction area is negligible outside the coil and magnetic cores.

As shown in Fig. 3(a), the direction of the arrows indicates the transfer path of the winding losses P_{winding} and core losses P_{core}, respectively. And the thermal network is established accordingly in Fig. 3(b). It is more refined than the thermal model of existing literature and the thermal resistance network considers the influence of internal convection and other thermal interface materials. The thermal resistance $R_{\mathrm{lw,hs-surf}}$ models the heat conduction from the hotspot inside the winding to the surface of the winding. $R_{\mathrm{fe,hs-surf}}$ models the heat conduction from the hotspot inside the ferrite to the surface of the ferrite cores. R_{pc} models the heat conduction from one side to the other side toward ferrite of potting compounds. Similarly, R_{cf}, R_{hma}, R_{pt}, R_{tp}, R_{ag}, and R_{ff} model the heat conduction from one side to another side of the coil frame, hot melt adhesive, polyimide tape, thermal pad, air gap, and ferrite fixture, respectively. R_{lcp} models the heat conduction from the vertical plane of heat source to the central vertical plane of the nearby coolant channel. $R_{\mathrm{lcp,cv}}$ models the heat convection between the wall of coolant channel and the liquid coolant. And $R_{\mathrm{ff,cv}}$ models the heat convection between the wall of ferrite fixture and the ambient.

Note that the temperature of liquid coolant is not always constant, as the coolant passes through more components, its temperature increases gradually. And the temperature rise from the inlet to the specific position can be calculated by the following formula.

$$T_{liquid} - T_{inlet} = \sum P_i \Big/ c_p \dot{m} \tag{22}$$

where $\sum P_i$ is the sum of power losses of the components that have been passed through, $\dot{m}$ and c_p are the mass flow and specific heat at a constant pressure of the liquid coolant.

By calculation, it is obvious that most winding losses and core losses are transferred down to the liquid cold plate by conduction, and taken away by coolant, while the heat dissipation to the air inside the shell is little. The main heat transfer path is shown as solid arrows, while other paths are shown as dotted arrows in Fig. 3(a). To further simplify the thermal network, the heat dissipation path of internal convection can be ignored. In addition, the thermal resistance with large values, such as $R_{\mathrm{ff,cv}}$ and $R_{\mathrm{cf,cv}}$, can be regarded as network breakpoints.

The complexity of thermal networks depends on the simplification of the temperature fields. In this study, it is assumed that the temperature of a magnetic component is

2332-7782 (c) 2021 IEEE. Personal use is permitted, but republication/redistribution requires IEEE permission. See http://www.ieee.org/publications_standards/publications/rights/index.html for more information.
Authorized licensed use limited to: Sintef. Downloaded on May 20,2022 at 10:23:19 UTC from IEEE Xplore. Restrictions apply.

This article has been accepted for publication in a future issue of this journal, but has not been fully edited. Content may change prior to final publication. Citation information: DOI 10.1109/TTE.2022.3175806, IEEE Transactions on Transportation Electrification

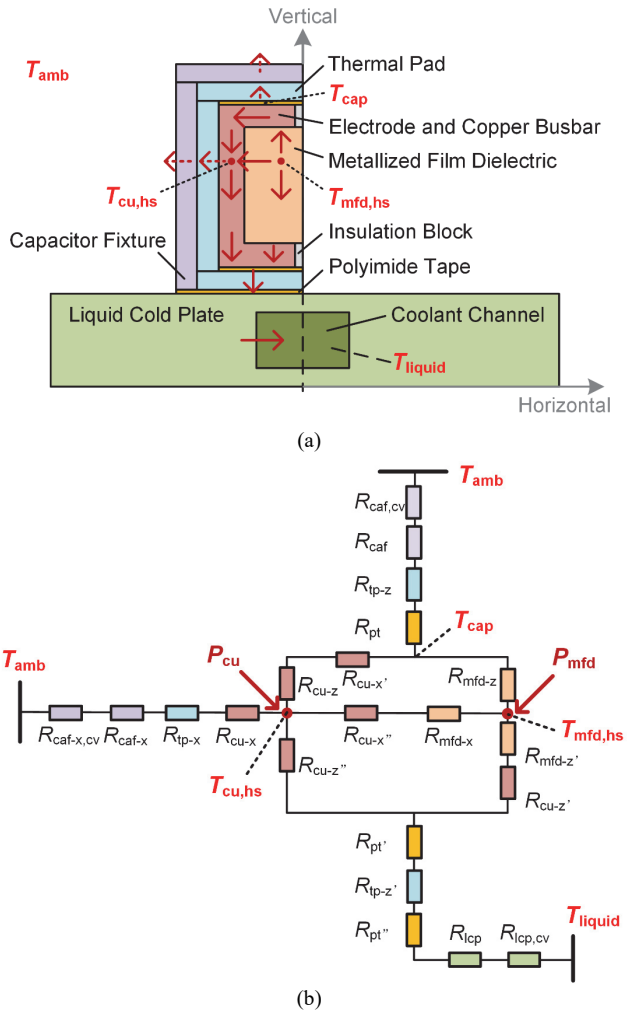

Fig. 4. Thermal analysis and modeling of capacitors in VA. (a) heat transfer path and (b) thermal network.

homogeneous in the horizontal plane. For example, ferrite cores are considered as a whole and are represented by a single node and modeled as two resistances. The temperature of the node represents the average temperature of cores. Considering the temperature is unequally distributed inside the magnetic component, or in the cases where the shape of coils and cores is complex and the loss distribution is nonuniform, the discretization of the model can be improved and the number of nodes can be increased. The corresponding algebraic equations need to be solved numerically. Such refined thermal networks are beyond the scope of this paper.

2) *Compensation Capacitors of VA*

The structure of capacitors, as well as the coolant channel below, is basically symmetric with respect to the central plane (as shown by the red dotted line in Fig. 2 (a)). Therefore, only the left side of a capacitor is analyzed. Considering both electrodes and busbars are made of pure copper, they are regarded as a whole. We estimate that 50% of capacitor bank losses are evenly distributed in the dielectric and others are distributed evenly in copper electrodes and busbars. They are regarded as point heat sources and are applied to the hotspots

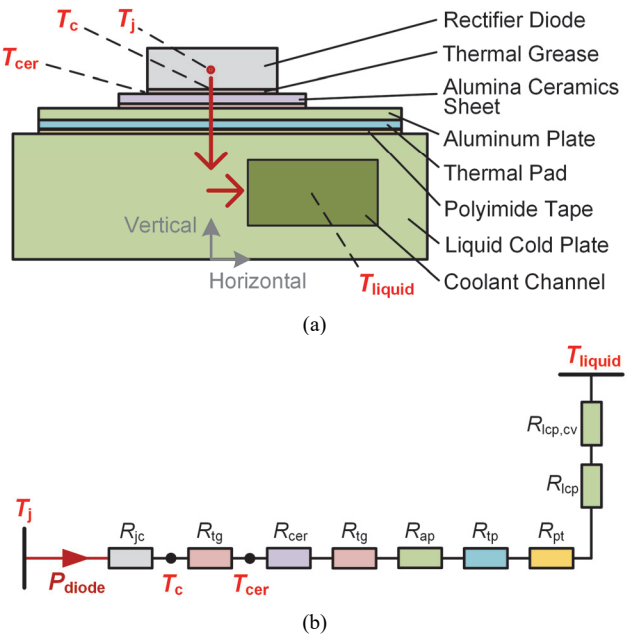

Fig. 5. Thermal analysis and modeling of rectifier diodes in VA. (a) heat transfer path and (b) thermal network.

inside the material, and the hotspot temperatures are $T_{\mathrm{mfd,hs}}$ and $T_{\mathrm{cu,hs}}$, respectively.

The heat transfer path of dielectric loss and copper loss is illustrated in Fig. 4(a). Most of the heat is transferred to the liquid cold plate and only a small fraction of the heat is transferred to the air inside the enclosure by conduction and convection. It is similar to the case of winding and ferrite cores.

Fig. 4(b) shows the thermal network, where $R_{\mathrm{mfd-x}}$ models heat conduction of the metallized film dielectric in the horizontal plane, while $R_{\mathrm{mfd-z}}$ models heat conduction in the vertical plane. The same applies to the heat transfer of the capacitor fixture (caf), the thermal pad (tp), and the electrode and copper busbar (cu) in the horizontal plane (-x) and in the vertical plane (-z). $R_{\mathrm{caf-x,cv}}$ represents the convective thermal resistance between the surface of the capacitor fixture and the ambient in the horizontal plane, while R_{pt} and R_{caf} model the heat conduction from one side to the other of the polyimide tape and the capacitor fixture, respectively.

3) *Rectifier Diodes of VA*

To adapt to other rectifier modules and accommodate the changes of mounting holes, the rectifier diodes are mounted on a 4 mm-thick aluminum plate, between which thermal grease, alumina ceramics heat conducting sheets, and thermal grease are applied to enhance the heat-conducting effect. Besides, thermal pads are used between the aluminum plate and liquid cold plate. The junction temperature T_{j} is commonly regarded as the hotspot temperature of diodes. The heat transfer path and thermal network of a diode are illustrated in Fig. 5. R_{jc} models the thermal resistance from junction to the case, and it can be looked up in the datasheet. By calculation, it is evident that the thermal resistance of thermal pads and thermal grease (R_{tp} and R_{tg}) has a great effect on the temperature rise of the diodes, and

2332-7782 (c) 2021 IEEE. Personal use is permitted, but republication/redistribution requires IEEE permission. See http://www.ieee.org/publications_standards/publications/rights/index.html for more information.
Authorized licensed use limited to: Sintef. Downloaded on May 20,2022 at 10:23:19 UTC from IEEE Xplore. Restrictions apply.

This article has been accepted for publication in a future issue of this journal, but has not been fully edited. Content may change prior to final publication. Citation information: DOI 10.1109/TTE.2022.3175806, IEEE Transactions on Transportation Electrification

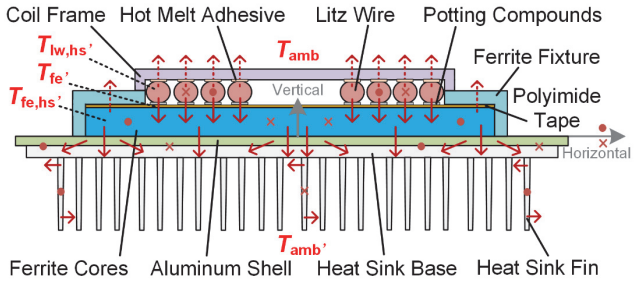

Fig. 6. Thermal analysis of the winding and cores in GA.

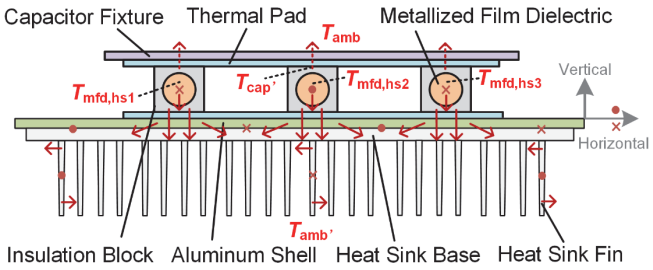

Fig. 7. Thermal analysis of the capacitors in GA.

attention should be paid to the choice of their material and thickness.

4) Litz Wire Winding and Ferrite Cores of GA

Liquid cooling relies on heat conduction and fluid convection to carry heat away, while inner air convection carries away limited heat. In contrast, the natural cooling method mainly relies on heat exchange between the heatsink fins and the ambient air.

The heat transfer path of the winding and cores in GA differs from that in VA. In VA, most of the heat is transferred to the adjacent liquid channel, and little is transferred horizontally to other heating components by the liquid cold plate. But in GA, heat needs to pass through the aluminum shell, then to the base plate of the heatsinks, and then to the fins. In this process, a greater proportion of the heat is conducted horizontally, including directions perpendicular to the paper, as shown in Fig. 6. In addition, considering the non-uniform distribution of heat sources, the heat flux at different positions is different even for the same fin.

Therefore, the assumptions of two-dimensional thermal networks and a single thermal resistance are not suitable here. Due to the complexity of three-dimensional thermal networks as described in part D.1), FEM is a better choice and the temperature distribution of GA can be obtained easily.

5) Compensation Capacitors of GA

In contrast to the capacitors in VA, the mounting conditions of the capacitor in GA are not symmetric concerning the central plane. The thermal analysis of the capacitor in GA is performed along with the red dashed line in Fig. 2(b), as shown in Fig. 7. Heat is conducted through the aluminum shell and heat sinks in all directions, and some of the heat is conducted to the aluminum shell below the winding, making it difficult to determine the value of heat sources in the thermal network. In addition, the value of thermal resistance of the aluminum shell and heat sinks cannot be simply quantified by equations.

Therefore, TNM is not suitable for the thermal modeling of GA. Instead, it is recommended to build a thermal FE model of GA including the winding, cores, and capacitors.

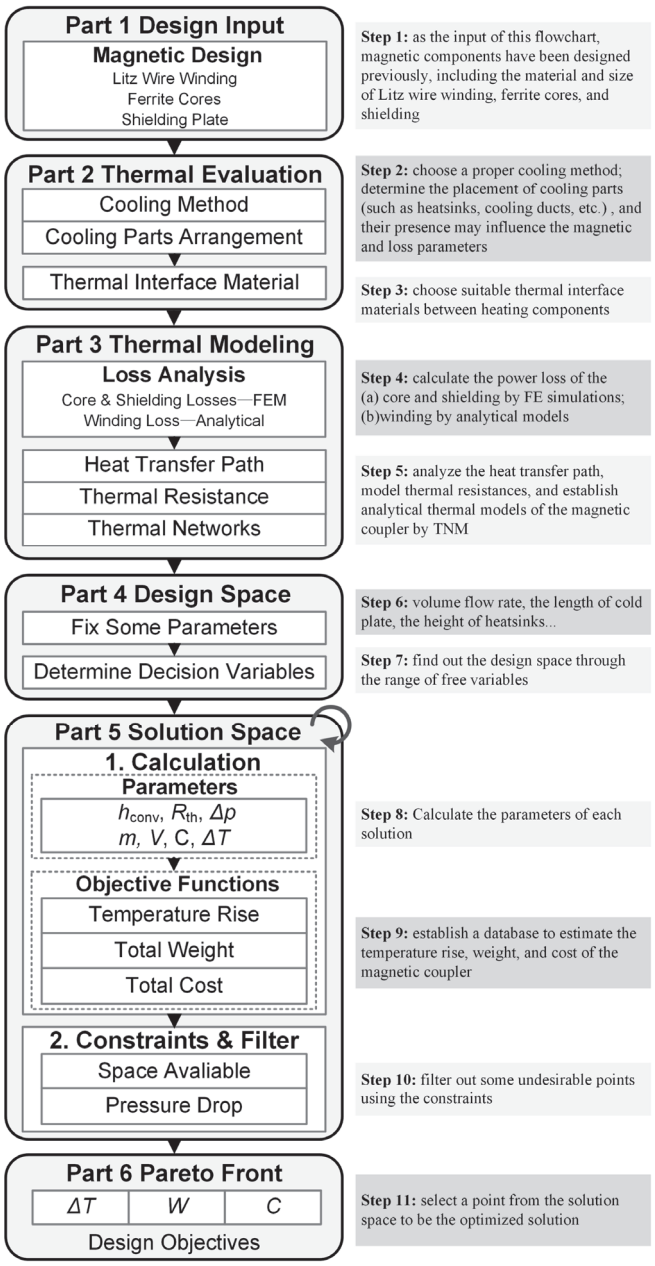

Fig. 8. Multi-objective thermal optimization procedure of magnetic couplers for EVs.

IV. Multi-Objective Thermal Optimization

Based on the presented model, multi-objective thermal optimization of the liquid-cooled magnetic coupler is conducted in this section. First, the conditions and main steps of the optimization procedure are outlined. Next, the results are presented to show the performance limit of the magnetic

2332-7782 (c) 2021 IEEE. Personal use is permitted, but republication/redistribution requires IEEE permission. See http://www.ieee.org/publications_standards/publications/rights/index.html for more information.
Authorized licensed use limited to: Sintef. Downloaded on May 20,2022 at 10:23:19 UTC from IEEE Xplore. Restrictions apply.

This article has been accepted for publication in a future issue of this journal, but has not been fully edited. Content may change prior to final publication. Citation information: DOI 10.1109/TTE.2022.3175806, IEEE Transactions on Transportation Electrification

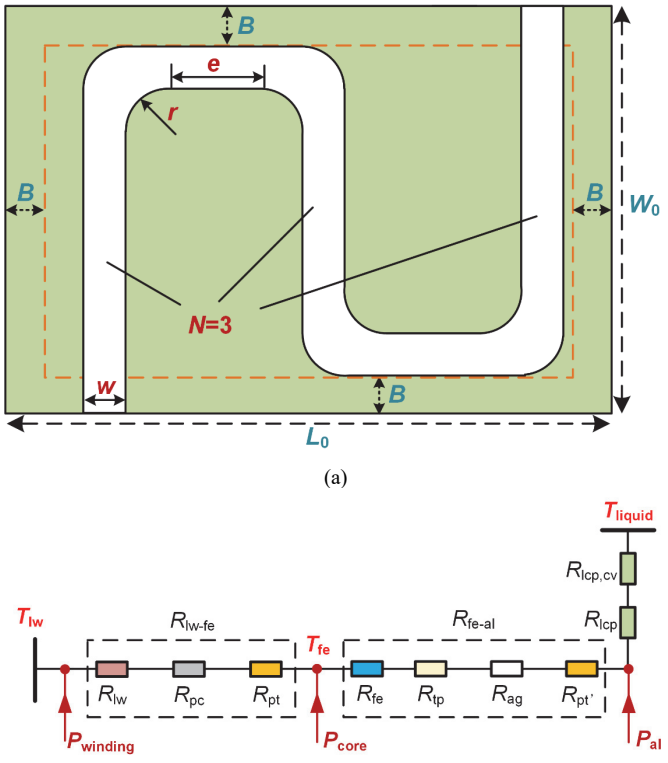

Fig. 9. (a) Fixed parameters and decision variables of the liquid cold plate (b) simplified thermal network of the magnetic coupler.

coupler. The Pareto tradeoff among temperature rise, weight, and cost is discussed, and a selected solution point and its parameter is given.

A. Multi-Objective Thermal Optimization Procedure of Magnetic Couplers for EVs

As shown in Fig. 8, the proposed procedure refers to and improves the optimization process presented in [9] and [37]. It focuses on the thermal aspect of magnetic couplers, considering the temperature rise, weight, and cost. Thermal design and optimization of the magnetic coupler are performed in terms of the design of the liquid cold plate and the selection of thermal interface materials.

B. Thermal Design Space for Liquid-Cooled Magnetic Coupler

As presented in Fig. 9(a), the length and width of the liquid cold plate are set as variable L_0 and W_0, respectively. Since a certain space is required between channels and the edge of the liquid cold plate, the minimum margin between them is set as B. The fixed parameters and operating conditions are summarized in Table V.

Besides, we define seven decision variables: the width of coolant channel w, the height of channel h, the number of channels N, the radius of bends r, the straight length e, the material of potting compounds p, and the material of thermal pads q. Fig. 9(a) shows the variables and parameters when N=3. Four optional potting materials are shown in Table VI. And two optional thermal pads are shown in Table VII. It is obvious that the cost or density for thermal interface materials with higher thermal conductivity is higher.

TABLE V
FIXED PARAMETERS AND OPERATING CONDITIONS

Var.	Description	Value
d_0	Thickness of cover plate	4 mm
L_0	Length of liquid cold plate	610 mm
W_0	Width of liquid cold plate	430 mm
B	Minimum marginal distance	60 mm
Q_v	Volume flow rate of the coolant	8 L/min
T_{inlet}	Inlet temperature	25℃

TABLE VI
OPTIONAL POTTING COMPOUNDS

p	Thermal Conductivity k_{pc} (W/m·K)	Weight Density ρ_{pc} (kg/m^3)	Cost ($/kg)
1	1	2350	15.0
2	1.5	2550	18.1
3	2	2800	46.5
4	3.3	3100	93.7

TABLE VII
OPTIONAL THERMAL PADS

q	Thermal Conductivity k_{tp} (W/m·K)	Weight m_{tp} (kg)	Cost C_{tp} ($)
1	3	0.528	7.1
2	6	0.528	18.9

The simplified thermal network of the liquid-cooled magnetic coupler is illustrated in Fig. 9(b), and it is used to calculate the temperature rise of materials. The hotspot of the winding/cores is located near the top surface of the winding/cores. This modification is reasonable, since the heat path to the cold plate has much lower thermal resistance compared to the convective path on top.

C. Objective Functions

1) Temperature rise

The primary goal of thermal design is to ensure the thermal feasibility of the system, and we want the temperature rise to be as low as possible. Therefore, the temperature rise is regarded as an objective function. In fact, temperature rise can be treated as a constraint in other optimization procedures, but it is not covered in this paper.

According to the proposed thermal network of the magnetic coupler, the temperature rise of the hotspot within the component follows:

$$\begin{aligned}\Delta T_{fe} &= T_{fe} - T_{inlet} \\ &= \left(P_{winding} + P_{core}\right)\left(R_{fe-al} + R_{lcp} + R_{lcp,cv}\right) \\ &\quad + P_{al}\left(R_{lcp} + R_{lcp,cv}\right) + \left(P_{winding} + P_{core} + P_{al}\right)\Big/ \dot{m}\cdot c_p \\ \Delta T_{lw} &= \Delta T_{fe} + P_{winding} R_{lw-fe}\end{aligned} \tag{23}$$

Since the hotspot temperature of the winding is always higher than that of cores, the temperature rise of the Litz wire is the main concern.

2332-7782 (c) 2021 IEEE. Personal use is permitted, but republication/redistribution requires IEEE permission. See http://www.ieee.org/publications_standards/publications/rights/index.html for more information.
Authorized licensed use limited to: Sintef. Downloaded on May 20,2022 at 10:23:19 UTC from IEEE Xplore. Restrictions apply.

This article has been accepted for publication in a future issue of this journal, but has not been fully edited. Content may change prior to final publication. Citation information: DOI 10.1109/TTE.2022.3175806, IEEE Transactions on Transportation Electrification

2) Weight of the magnetic coupler

Lightweight design is a trend for onboard wireless chargers, so the total weight of the magnetic coupler is treated as the objective function, which is the sum of the weights of individual materials. The weight of the liquid cold plate includes the weight of aluminum material and the weight of liquid coolant. The weight of the other components, including the hot melt adhesive, coil frame, ferrite fixture, and cover plate, is estimated at 2.54 kg.

$$m_{total} = m_{lw} + m_{pc} + m_{fe} + m_{tp} + m_{lcp} + m_{other} \tag{24}$$

$$m_{pc} = \rho_{pc} \cdot V_{pc} \tag{25}$$

$$m_{lcp} = \rho_{al}\left(W_0 \cdot L_0 \cdot \left(h + 2d_0\right) - w \cdot h \cdot L\right) + \rho \cdot w \cdot h \cdot L \tag{26}$$

3) Cost of the magnetic coupler

The total cost of the magnetic coupler is also important, and it is the sum of the cost of each material. The cost of the liquid cold plate can be divided into three parts: fixed cost, material cost, and processing cost. And the last item is related to the length and width of the channel.

$$C_{total} = C_{lw} + C_{pc} + C_{fe} + C_{tp} + C_{lcp} + C_{other} \tag{27}$$

$$C_{lcp} = C_{fixed} + C_{material} + C_{process} = 315 + 3.43\rho_{al}\left(L_0 \cdot W_0 \cdot \left(h + 2d_0\right)\right) + 157.5\left(L \cdot \left(50w + 0.5\right)\right) \tag{28}$$

The related fixed parameters of the materials are listed in Table VIII.

TABLE VIII
PARAMETERS FOR CALCULATION WEIGHT, VOLUME, AND COST

Var.	Description	Value
m_{lw}	Weight of Litz wire winding	2.33 kg
m_{fe}	Weight of ferrite cores	15.48 kg
m_{other}	Weight of other components	2.54 kg
V_{pc}	Volume of potting compounds	0.00028 m^3
C_{lw}	Cost of Litz wire winding	$ 65.52
C_{fe}	Cost of ferrite cores	$ 276.42
C_{other}	Cost of other components	$ 101

D. Constraints

The space limitation mentioned before is the first constraint, meaning that the channel layout cannot exceed the available space. Another constraint is employed according to the requirement of the cooling system: the maximum pressure drop of liquid coolant is set at 10 kPa.

E. Optimization Model

The multi-objective optimization model consists of the objective functions, decision variables, and constraints. They are shown below. The range of channel width and height are determined by the strength requirements of the shell of VA, and limited by the processing technic.

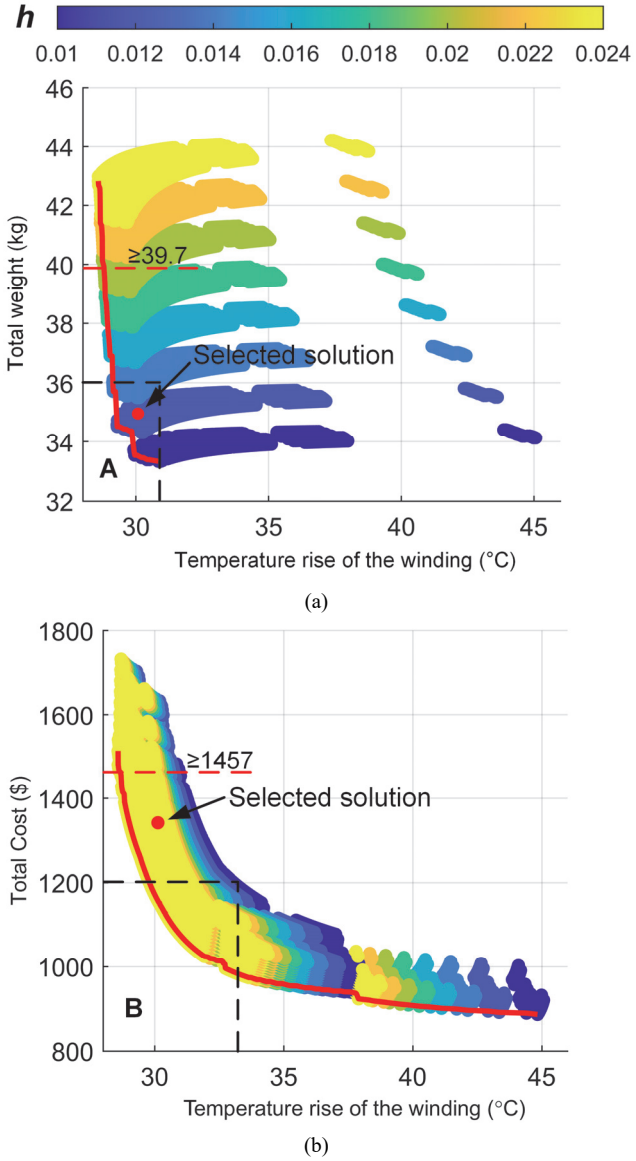

Fig. 10. The results of eligible 325,728 designs, with the red lines representing Pareto front.

$$OBJECTIVES: \begin{cases} \Delta T = f_1\left(w,h,N,r,e,p,q\right) \\ m = f_2\left(w,h,N,r,e,p,q\right) \\ C = f_3\left(w,h,N,r,e,p,q\right) \end{cases} \tag{29}$$

$$DESION-SPACE: \begin{cases} w = \left[0.01:0.001:0.02\right] \\ h = \left[0.01:0.002:0.024\right] \\ N = [1:1:10] \\ r = [0.005:0.005:0.05] \\ e = [0.01:0.01:0.1] \\ p = [1,2,3,4] \\ q = [1,2] \end{cases} \tag{30}$$

2332-7782 (c) 2021 IEEE. Personal use is permitted, but republication/redistribution requires IEEE permission. See http://www.ieee.org/publications_standards/publications/rights/index.html for more information.
Authorized licensed use limited to: Sintef. Downloaded on May 20,2022 at 10:23:19 UTC from IEEE Xplore. Restrictions apply.

This article has been accepted for publication in a future issue of this journal, but has not been fully edited. Content may change prior to final publication. Citation information: DOI 10.1109/TTE.2022.3175806, IEEE Transactions on Transportation Electrification

TABLE IX
VARIABLES AND PARAMETERS OF THE SELECTED SOLUTION

	W(mm)	h (mm)	N	r (mm)	e (mm)	p	q	Δp (Pa)	C_{to} (\$)	m_{to} (kg)	ΔT_{lw} (°C)
Solution	16	12	6	20	38	4	2	5013	1366.7	35.16	30.26

TABLE X
OPERATING CONDITIONS OF THE IPT SYSTEM

Parameter	Value
Ambient temperature (°C)	25
Inlet liquid coolant temperature (°C)	25
Inner ambient temperature (°C)	50
Inner convection coefficient (W/m·K)	2
Natural convection coefficient (W/m·K)	6 [38]
Liquid coolant flow rate (L/min)	8

$$CONSTRAINTS: \begin{cases} g_1: space\ available \\ g_2: \Delta p < 10\,kPa \end{cases} \tag{31}$$

F. Calculation Results and the Selected Solution Point

There are 704,000 combinations in total. Except for the designs violating constraints, the results of the remaining 325,728 combinations are shown in Fig. 10. The height of channel is an important variable affecting the total weight and cost. Any point on the Pareto front is considered "Pareto optimal". For example, in Fig. 10(a), the temperature rise of the designs on the Pareto front could be minimized at the expense of weight, or the weight could be minimized at the expense of temperature rise, while it is impossible to decrease both temperatures rise and weight at the same time, which is described as a trade-off between temperature rise and weight. A similar tradeoff also exists between temperature rise and cost.

Although the Pareto fronts have been obtained, the selection of optimal solution points needs further discussion, because it is a multi-objective optimization problem. Taking the design points on the Pareto front in area A of Fig. 10(a) as examples, their weight and temperature are relatively low, but their cost all exceeds \$1457. For the design points on the Pareto front in area B, their cost and temperature are relatively low, but their weight all exceeds 39.7 kg. Therefore, they are not the desired design points. After the tradeoff among temperature rise, weight, and cost, an optimized solution point is selected as shown in Fig. 10. Specifically, more attention is paid to the weight and temperature rise. Its variables and parameters are summarized in Table IX.

V. STUDY ON THERMAL PERFORMANCE OF THE SYSTEM WITH FEM

The thermal performance of the IPT system is studied in this section. The thermal FE models are established and the results are compared with those obtained by TNM. Then, the thermal performance of the system at different power levels and misaligned conditions is analyzed. Finally, FEM and TNM are compared from two aspects.

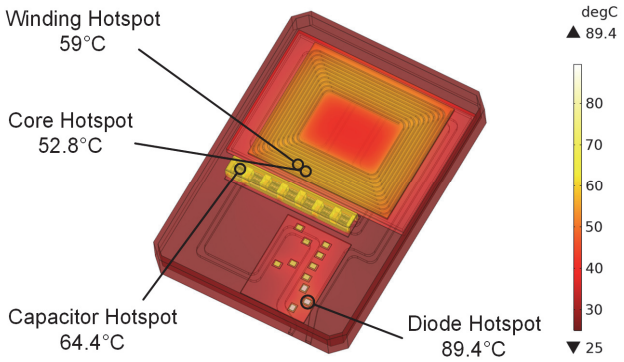

Fig. 11. Temperature distribution and hotspots of VA at P0 by FEM (the loss corresponding to a 60A-RMS current is considered as P0).

A. Thermal Analysis and Modeling Based on FEM

Thermal FE models of VA and GA are established and the simulation is carried out. To reduce the number of simulations required, the feedback of the calculated component temperatures to the power loss calculation is not included. Water is selected as the liquid coolant in the simulation and the prototype experiment. In addition, the algebraic model of turbulence Y+ is used because of low calculated strength and a good approximation of the internal flow. The losses in FE models are uniformly distributed in the volume of winding, cores, capacitors, and aluminum shells in the form of heat sources, which is different from the point-type heat sources in the thermal networks. The designed cold plate model in this paper is verified by simulation, with the pressure drop and the temperature rise of the coolant below the limit.

The operating conditions of the IPT system are summarized in Table X. The initial temperature of these components is set at 25°C. And the highest temperature of each component is selected as its hotspot temperature. The liquid coolant flow rate is based on the available rated flow rate of the liquid cold plate from the cooling system of the EV. For convenience, the 60A-RMS current is set as the rated operating condition for the maximum output power at the aligned position, and its corresponding loss is considered P0. Fig. 11 illustrates the temperature distribution and hotspots of each component in VA at P0.

The capacitor on the left is hotter because the coolant below is slowly increasing in temperature as it moves from right to left along the coolant channel. It should be noted that for the heating components, most of the heat is taken away by the coolant inside the channel below them, but there is still some heat that is conducted to other locations by the aluminum cold plate. Therefore, the temperature of the winding and ferrite cores close to the compensation capacitors is higher than that far away. This is inconsistent with the aforementioned assumption that the components are basically independent. However, the temperature difference within the same component is several degrees at most, and a margin of 10°C can be reserved in the thermal design.

2332-7782 (c) 2021 IEEE. Personal use is permitted, but republication/redistribution requires IEEE permission. See http://www.ieee.org/publications_standards/publications/rights/index.html for more information.
Authorized licensed use limited to: Sintef. Downloaded on May 20,2022 at 10:23:19 UTC from IEEE Xplore. Restrictions apply.

This article has been accepted for publication in a future issue of this journal, but has not been fully edited. Content may change prior to final publication. Citation information: DOI 10.1109/TTE.2022.3175806, IEEE Transactions on Transportation Electrification

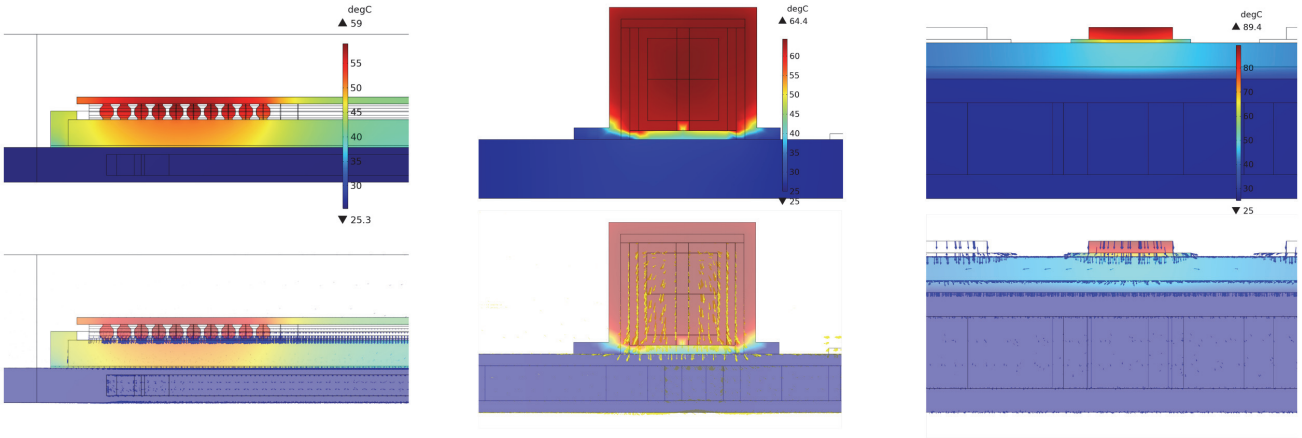

Fig. 12. Temperature distribution and arrows which represent heat flux on the cross-section of (a) the winding and cores, (b) the capacitor, and (c) the diode in VA.

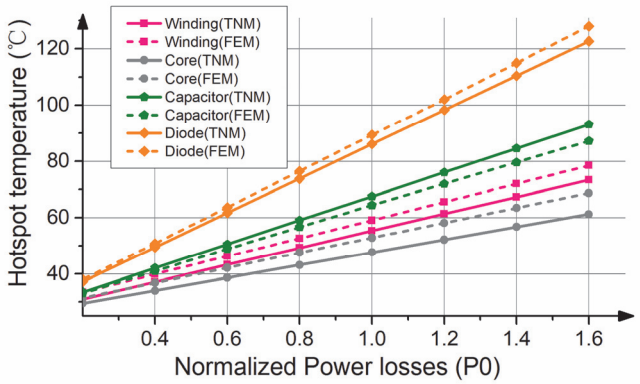

Fig. 13. Hotspot temperature in VA obtained by TNM and FEM with the normalized power losses.

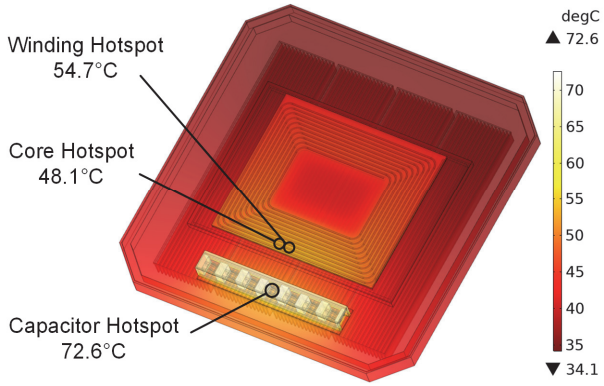

Fig. 14. Temperature distribution of GA at P0 by FEM.

Fig. 12 shows the temperature distribution as well as the heat flux on cross-sections of the heating components. It is very similar to the previous analysis, which proves the rationality of thermal analysis and thermal modeling. There are few arrows on the surfaces of the coil frame or the capacitor fixture because very little heat is transferred through them.

For simplicity, the loss is considered proportional to the quadratic of the current. Therefore, as the current increases, the proportion of the loss of each component in the total loss remains constant. As shown in Fig. 13, the hotspot temperature of components in VA varying with the normalized power losses is shown in Fig. 13. Approximatively, whether by TNM or FEM, the obtained hotspot temperature increases linearly with power losses. And the difference between the two methods also increases slightly along with the losses, but the average difference is less than 10% and the accuracy is acceptable.

The temperature of GA at P0 is shown in Fig. 14. Fig. 15 shows the sectional temperature in GA. The temperature varies greatly at different positions. For example, the temperature difference within the winding is more than ten degrees. Therefore, the assumption that nodes represent the average temperature is no longer applicable. FEM has more advantages than a two-dimensional thermal resistance network in this regard.

B. Analysis of Different Power Levels and Coil Misalignments

The maximum cooling capacity of the system determines the maximum power loss and current of the system. As soon as the maximum power loss or current is reached during operation, the only option is to limit the coil current by decreasing the output power. In this part, the limits of output power and efficiency, as well as misalignment tolerance of the system, are discussed.

The fitting formulas of temperature and loss are derived from Fig. 13 for subsequent analysis. Note that the thermal limit of ABS plastic is regarded as that of the winding and cores, because it is lower (80°C).

By fitting formulas, the maximum current of each component within thermal limits is calculated and summarized in Table XI. The maximum RMS current in VA and GA is considered as 77 A and 70 A, respectively. In other words, they correspond to 1.65 P0 and 1.35 P0, respectively. At this time, the ferrite does not exceed the saturation limit, and it is verified by FE simulations. Since the thermal limit of the system has been derived, then the temperature rise of heating components in VA and GA at different power levels and efficiency are discussed, as illustrated in Fig. 16. The red line represents the limit of temperature rise.

Fig. 17 illustrates the two-dimensional view of the thermal limits of each component. The capacity of the cooling system

2332-7782 (c) 2021 IEEE. Personal use is permitted, but republication/redistribution requires IEEE permission. See http://www.ieee.org/publications_standards/publications/rights/index.html for more information.
Authorized licensed use limited to: Sintef. Downloaded on May 20,2022 at 10:23:19 UTC from IEEE Xplore. Restrictions apply.

This article has been accepted for publication in a future issue of this journal, but has not been fully edited. Content may change prior to final publication. Citation information: DOI 10.1109/TTE.2022.3175806, IEEE Transactions on Transportation Electrification

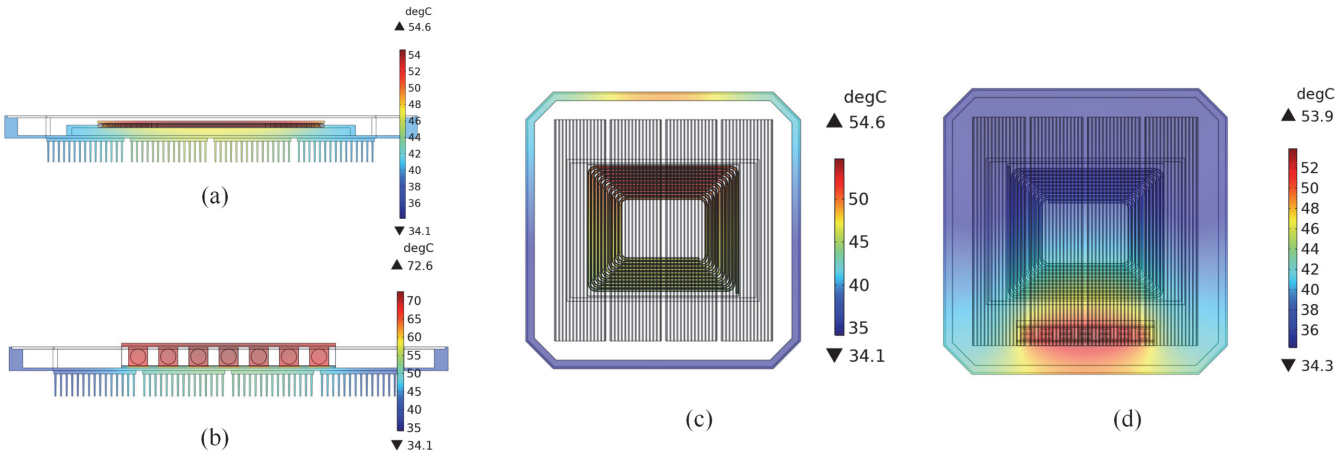

Fig. 15. Temperature distribution on (a) the cross-section of the winding and cores, (b) the cross-section of capacitors, (c)the horizontal section of the winding, and (d) the horizontal section of the aluminum plate in GA.

TABLE XI
THE MAXIMUM CURRENT OF EACH COMPONENT WITHIN THERMAL LIMITS BY FITTING FORMULAS

	VA				GA		
	Winding	Core	Capacitor	Diode	Winding	Core	Capacitor
TNM	81 A	93 A	74 A	94 A	\	\	\
FEM	77 A	85 A	77 A	91 A	81 A	91 A	70 A

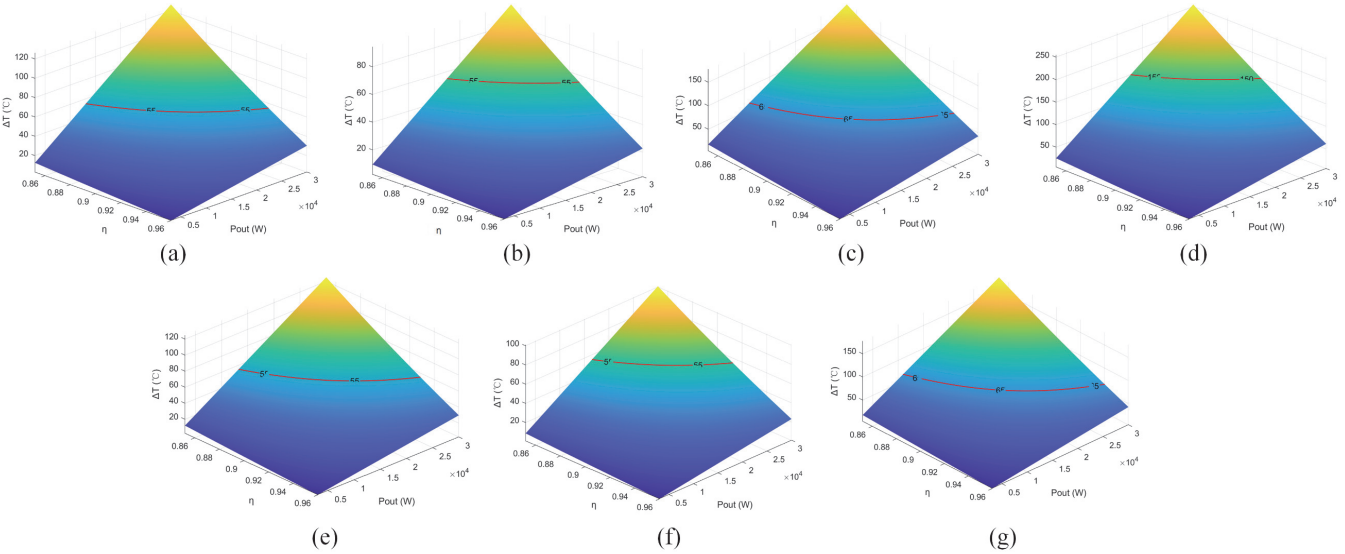

Fig. 16. Temperature rise of heating components at different power levels and efficiency. (a)the winding, (b) cores, (c) capacitors, and (d) diodes in VA; (e) the winding, (f) cores, and (g) capacitors in GA.

determines the maximum output power and the minimum efficiency of the system. The lower right area of the lines which represent the thermal limits is the feasible region. And the capacitors in GA are most likely to reach the thermal limit.

Next, misalignment tolerance is studied. Fig. 18 shows an example of the temperature distribution of GA at the misaligned position (1.35P0). In practice, misalignments between GA and VA are inevitable when drivers try to move the vehicle aligned to the center of the wireless charging spot. As a penalty for lower magnetic coupling, a larger primary current is required to maintain the rated output power. When the battery voltage is stable and the output power is constant, the current in the receiving coil remains unchanged. As derived from (5), the current in the transmitting coil increases to maintain the rated output power as the mutual inductance degrades, while the dc-link voltage of the transmitter side decreases. The RMS current of transmitting coils with misalignment along the Y-axis is shown in Fig. 19. The misalignment tolerance of the IPT system is about 70 mm, and it is determined by the data in Table XI. If the misalignment exceeds this limit, the output power needs to be reduced for safety's sake.

C. Comparison Between Modeling Methods

As mentioned in the previous sections, the temperature

2332-7782 (c) 2021 IEEE. Personal use is permitted, but republication/redistribution requires IEEE permission. See http://www.ieee.org/publications_standards/publications/rights/index.html for more information.
Authorized licensed use limited to: Sintef. Downloaded on May 20,2022 at 10:23:19 UTC from IEEE Xplore. Restrictions apply.

This article has been accepted for publication in a future issue of this journal, but has not been fully edited. Content may change prior to final publication. Citation information: DOI 10.1109/TTE.2022.3175806, IEEE Transactions on Transportation Electrification

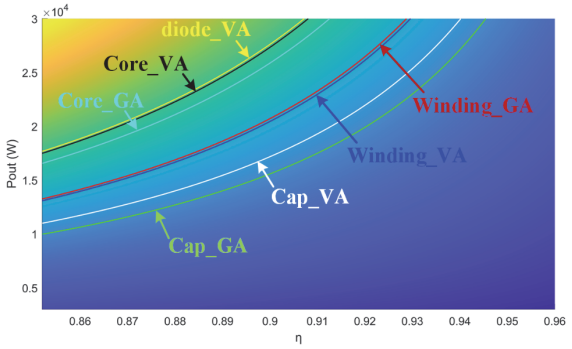

Fig. 17. Two-dimensional view of the thermal limits for heating components.

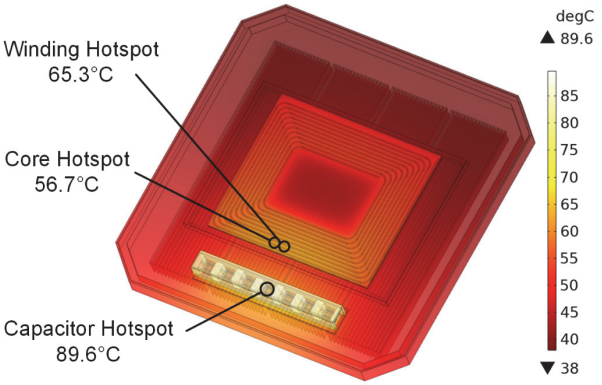

Fig. 18. Temperature distribution of GA at the misaligned position (at 1.35P0).

distribution can be visualized by FEM, while the key thermal resistance is easily identified by TNM, which is conducive to optimizing the thermal design schemes. This part compares and discusses the thermal modeling methods between TNM and FEM from other two aspects.

1) Calculation Time

Calculation time is very important during the thermal design stage, where the parameters change constantly. In this aspect, TNM has obvious advantages for liquid-cooled IPT-based systems. Taking the model of VA in this paper as an example, TNM uses programs written in MATLAB, while FEM depends on the multi-physical field model based on solid and fluid heat transfer, as well as the algebraic model of turbulence Y+ by COMSOL Multiphysics 5.5. Assuming the programs and the FE model have been built, the average time to run the optimization programs is 40 minutes, and the calculation time for a certain solution point is less than 3 seconds. On the contrary, the average simulation time is 132 minutes with the FE software. The reason is that turbulence simulation consumes major computational resources. It is also possible to do FEM without including CFD for VA, and this would reduce the problem to one of conduction heat transfer, same as for the GA.

For GA, its internal fluid flow simulation is not required, and the external convective heat transfer coefficient is given by referring to tables or empirical formulas. Therefore, its essence is solid heat transfer, and it takes only 38 seconds to simulate.

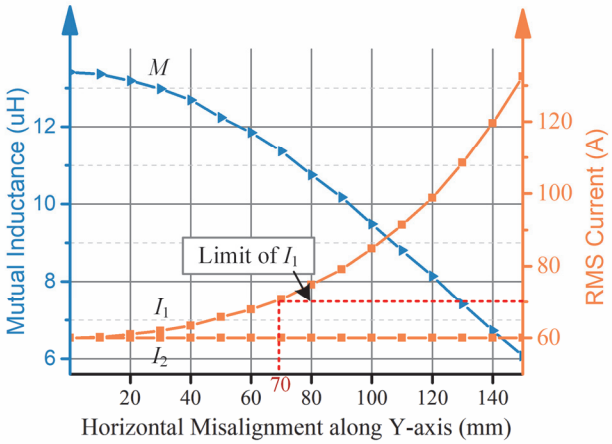

Fig. 19. Mutual inductance and RMS current with horizontal misalignment along the Y-axis.

2) Applicable Scenarios

TNM is more suitable for systems with a simple shape, symmetrical structure, and uniform loss distribution. Even simplified two-dimensional thermal networks have acceptable accuracy; otherwise, FEM may be a better choice.

VI. Experimental Verification

For validation purposes, VA and GA prototypes were built, as shown in Fig. 20. Fiber Bragg grating (FBG) temperature sensors were used for the advantages of not having electromagnetic field disturbance and complete coverage of the measurement area [39].

Along with thermocouples, these sensors were glued to the Litz wire, ferrite cores, capacitor, and ceramics sheet. The position of measurement points is shown in Fig. 3-7 and Fig. 20, six points in total. Because of the restriction of the measuring devices, we could only obtain the temperature of the material surface or the temperature of adjacent components, rather than the hotspot temperature inside the material. Then we built the experiment setup, as shown in Fig. 21. The operating conditions were consistent with those of the FE model.

During the first few minutes of start-up, the output power gradually increased, reaching the maximum value (28.6 kW) in about 4 minutes. And the dc-dc efficiency was as high as 95.9%. After that, the output power decreased slightly and fluctuated around 28 kW. Fig. 22 shows the temperature variation at the measurement points over time. Since the temperature indicated no increase or decrease greater than 1°C within successive readings from the 32nd minute to the 35th minute, we thought that the system became basically stable at the 35th minute. The values were approximately determined as the final working temperature of the components.

The temperature obtained by TNM, FEM, and the experiment at the measurement points is summarized and compared in Fig. 23. Data shows good agreement and the maximum error between the two calculation methods and the experiment is less than 10%. Considering the simplification and approximation when modeling, the accuracy is deemed to be at

2332-7782 (c) 2021 IEEE. Personal use is permitted, but republication/redistribution requires IEEE permission. See http://www.ieee.org/publications_standards/publications/rights/index.html for more information.
Authorized licensed use limited to: Sintef. Downloaded on May 20,2022 at 10:23:19 UTC from IEEE Xplore. Restrictions apply.

This article has been accepted for publication in a future issue of this journal, but has not been fully edited. Content may change prior to final publication. Citation information: DOI 10.1109/TTE.2022.3175806, IEEE Transactions on Transportation Electrification

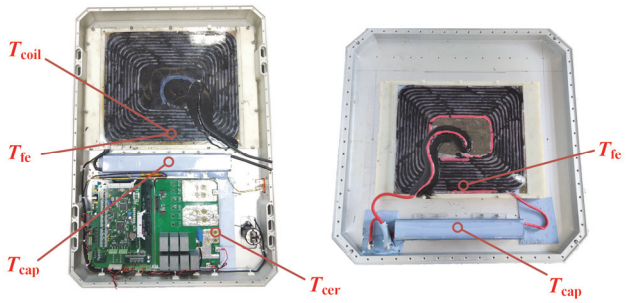

Fig. 20. Experimental prototypes of (a) VA and (b) GA.

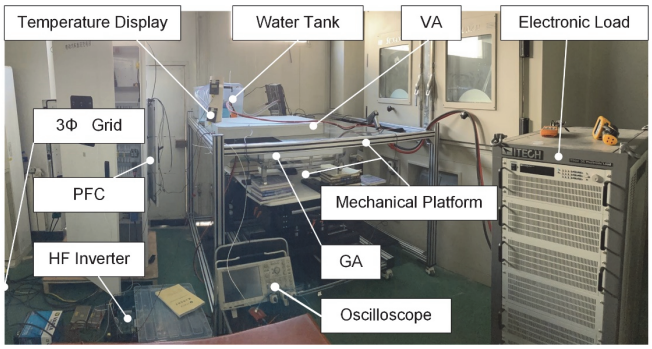

Fig. 21. Experimental setup.

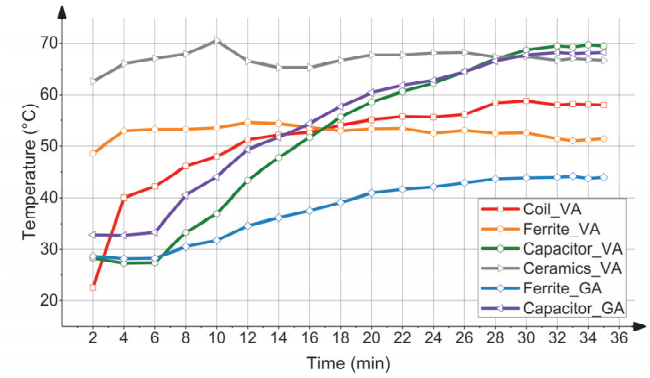

Fig. 22. Temperature at measurement points with time.

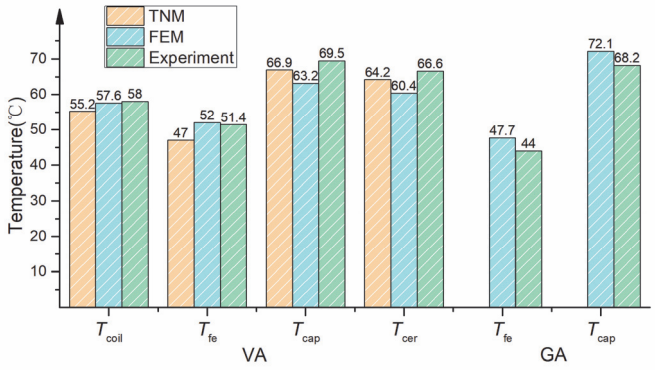

Fig. 23. Temperature at the measured position by TNM, FEM, and experiment.

TABLE XII
COMPARISON OF EXISTING WORKS

Reference	[8-10]	[13]	[14]	[15]	[21-23]	Proposed
P (kW)	5/50	6.6	6.6	11	10	30
Method	A+S	(A)+S	S	S	S	A+S
Thermal networks	Calculable Simplified	Schematic Simplified	/	/	/	Calculable Detailed
Thermal FE models	Simplified	Simplified	Simplified	Detailed	Simplified	Detailed
Cooling	Natural air/Forced air	Natural air	Natural air	Natural air + Forced air	Natural air	Liquid coolant + Natural air
Misalignment	Considered	Ignored	Considered	Ignored	Ignored	Considered
Computational time	/	/	/	/	7 h	VA: 3 s /132 min GA: 38 s
Maximum error (%)	23.3	6.6	9.2	16.3	10.0	9.3

A-Analytical, S-Simulations

TABLE XIII
THE THEORETICAL MAXIMUM POWER DENSITY OF THE PROTOTYPE

	P_m (kW)	Size (L×W×H, dm)	Actual weight (kg)	Gravimetric power density (kW/kg)	Area-related power density (kW/dm^2)	Volumetric power density (kW/dm^3)
VA (liquid-cooled)	50	4.3×6.1×0.85	38.5	1.30	1.91	2.24
GA (naturally cooled)	40	8.0×8.0×0.92	42.6	0.94	0.63	0.68

Only the liquid cold plate below the magnetic coupler is considered. P_m represents the power corresponding to the tolerant maximum loss.

an acceptable level.

The proposed work is compared with existing schemes in Table XII. Our proposed analytical model is more accurate than previous analytical models. It takes less time to calculate compared to FE models. Besides, this is the first paper to study liquid-cooled IPT systems, and it also considers the thermal limit and misalignment tolerance of the system.

The theoretical maximum power density of the prototype is shown in Table XIII. P_m represents the power corresponding to the maximum loss that can be borne. For a fair comparison, only the liquid cold plate below the magnetic coupler is considered. Due to the sides of the shell, the actual weight is a bit heavier than the total weight calculated before. Because the surface of GA and the weight of heatsinks are large, the air-cooled GA has a lower power density.

2332-7782 (c) 2021 IEEE. Personal use is permitted, but republication/redistribution requires IEEE permission. See http://www.ieee.org/publications_standards/publications/rights/index.html for more information.
Authorized licensed use limited to: Sintef. Downloaded on May 20,2022 at 10:23:19 UTC from IEEE Xplore. Restrictions apply.

This article has been accepted for publication in a future issue of this journal, but has not been fully edited. Content may change prior to final publication. Citation information: DOI 10.1109/TTE.2022.3175806, IEEE Transactions on Transportation Electrification

VII. Conclusion

The thermal design and optimization of a 30 kW IPT system for EVs are presented in this paper. In this process, improved analytical thermal networks were proposed with more detailed models and accurate results. The temperature by TNM showed good agreement with that by FE models and the experiment, verifying the thermal models. Based on the presented thermal network, the multi-objective thermal optimization procedure was conducted. It revealed the Pareto tradeoffs and performance limitations in terms of temperature rise, weight, and cost for the liquid-cooled magnetic coupler. The proposed thermal networks and optimization procedure facilitate faster optimization of magnetic couplers, and provide a useful tool to achieve lightweight and high-power for IPT systems.

References

[1] S. Jia, C. Chen, S. Duan, and Z. Chao, "Dual-side asymmetrical voltage-cancellation control for bidirectional inductive power transfer systems," *IEEE Trans. Ind. Electron.*, vol. 68, no. 9, pp. 8061–8071, Sep. 2020.

[2] H. Feng, R. Tavakoli, and O. C. Onar, "Advances in high-power wireless charging systems: overview and design considerations," *IEEE Trans. Transp. Electrific.,* vol. 6, no. 3, pp. 886-919, July. 2020.

[3] J. Yuan, L. Dorn-Gomba, A. D. Callegaro, J. Reimers, and A. Emadi, "A review of bidirectional on-board chargers for electric vehicles," *IEEE Access*, vol. 9, pp. 51501–51518, Mar. 2021.

[4] E. Snelling, "Power Transformers," in *Soft Ferrites Properties and Applications*. 1st ed., London, England: Iliffe Books Ltd, 1969, pp. 303-305.

[5] R. Petkov, "Optimum design of a high-power, high-frequency transformer," *IEEE Trans. Power Electron.*, vol. 11, no. 1, pp. 33–42, Jan. 1996.

[6] V. C. Valchev and A. Van den Bossche, "Thermal Aspects," in *Inductors and Transformers for Power Electronics*, 1st ed. Florida, USA: CRC Press, 2005, pp. 258-263.

[7] J. Itoh, K. Mizoguchi, L. H. Nam, and K. Kusaka, "Design method of cooling structure considering load fluctuation of high-power wireless power transfer system," in *2019 IEEE 4th International Future Energy Electronics Conference (IFEEC)*, Singapore, Singapore, Nov. 2019, pp. 1–6.

[8] R. Bosshard, J. W. Kolar, J. Muhlethaler, I. Stevanovic, B. Wunsch, and F. Canales, "Modeling and η-α-pareto optimization of inductive power transfer coils for electric vehicles," *IEEE J. Emerg. Sel. Top. Power Electron.*, vol. 3, no. 1, pp. 50–64, Mar. 2015.

[9] R. Bosshard, "Multi-objective optimization of 50 kW/85 kHz IPT system for public transport," *IEEE J. Emerg. Sel. Top. Power Electron.*, vol. 4, no. 4, pp. 1370-1382, Aug. 2016.

[10] R. Bosshard, "Multi-objective optimization of inductive power transfer systems for EV charging," Ph.D. dissertation, Dept. Elect. ETH, Zurich., ZH., 2015.

[11] V. Kindl, R. Pechanek, M. Zavrel, T. Kavalir, and P. Turjanica, "Inductive coupling system for electric scooter wireless charging: electromagnetic design and thermal analysis," *Electr. Eng.*, vol. 102, no. 1, pp. 3–12, Mar. 2020.

[12] C. Zhu *et al.*, "Thermal simulation and optimization study for magnetic coupler of static electric vehicle wireless power transfer systems," in *the 22nd International Conference on Electrical Machines and Systems (ICEMS)*, Harbin, China, Sep. 2019.

[13] C. Liang *et al.*, "Modeling and analysis of thermal characteristics of magnetic coupler for wireless electric vehicle charging system," *IEEE Access*, vol. 8, pp. 173177–173185, Sep. 2020.

[14] S. Niu, H. Yu, S. Niu, and L. Jian, "Power loss analysis and thermal assessment on wireless electric vehicle charging technology: The over-temperature risk of ground assembly needs attention," *Appl. Energy*, vol. 275, Oct. 2020, Art. no. 115344.

[15] S. Zimmer, M. Helwig, P. Lucas, A. Winkler, and N. Modler, "Investigation of thermal effects in different lightweight constructions for vehicular wireless power transfer modules," *World Electr. Veh. J.*, vol. 11, no. 4, Oct. 2020. Art. no. 67.

[16] M. Mohammad, O. C. Onar, J. L. Pries, V. P. Galigekere, G.-J. Su, and J. Wilkins, "Thermal analysis of a 50 kW three-phase wireless charging system," in *2021 IEEE Transportation Electrification Conference & Expo (ITEC)*, Chicago, IL, USA, Jun. 2021, pp. 1–6.

[17] C. Kaufmann *et al.*, "Efficient frequency-transient co-simulation of coupled heat-electromagnetic problems," *J. Math. Ind.*, vol. 4, no. 1, Dec. 2014, Art. no. 1.

[18] T. Campi, S. Cruciani, V. De Santis, and M. Feliziani, "EMF safety and thermal aspects in a pacemaker equipped with a wireless power transfer system working at low frequency," *IEEE Trans. Microw. Theory Tech.*, vol. 64, pp. 375-382, Feb. 2016, Art. no. 2.

[19] M. Alsayegh, M. Saifo, M. Clemens, and B. Schmuelling, "Magnetic and thermal coupled field analysis of wireless charging systems for electric vehicles," *IEEE Trans. Magn.*, vol. 55, no. 6, pp. 1–4, Jun. 2019.

[20] R. Wojda, V. P. Galigekere, J. Pries, and O. Onar, "Thermal analysis of wireless power transfer coils for dynamic wireless electric vehicle charging," in *2020 IEEE Transportation Electrification Conference & Expo (ITEC)*, Jun. 2020, pp. 835–838.

[21] S. Kim, M. Amirpour, G. Covic, and S. Bickerton, "Thermal characterisation of a double-d pad," in *2019 IEEE PELS Workshop on Emerging Technologies: Wireless Power Transfer (WoW)*, London, United Kingdom, Jun. 2019, pp. 1–5.

[22] M. Amirpour, S. Kim, M. P. Battley, P. Kelly, S. Bickerton, and G. Covic, "Coupled electromagnetic-thermal analysis of roadway inductive power transfer pads within a model pavement," *Appl. Therm. Eng.*, vol. 189, May. 2021, Art. no. 116710.

[23] S. Kim *et al.*, "Thermal evaluation of an inductive power transfer pad for charging electric vehicles," *IEEE Trans. Ind. Electron.*, vol. 69, no. 1, pp.314-322, Jan. 2022.

[24] N. Rasekh, S. Dabiri, N. Rasekh, M. Mirsalim, and M. Bahiraei, "Thermal analysis and electromagnetic characteristics of three single-sided flux pads for wireless power transfer," *J. Clean. Prod.*, vol. 243, Jan. 2020, Art. no. 118561.

[25] M. Moghaddami and A. Sarwat, "Time-dependent multi-physics analysis of inductive power transfer systems," in *2018 IEEE Transportation Electrification Conference and Expo (ITEC)*, Long Beach, CA, USA, Jun. 2018, pp. 130–134.

[26] S. Jayalath and A. Khan, "Design, challenges, and trends of inductive power transfer couplers for electric vehicles: a review," *IEEE J. Emerg. Sel. Top. Power Electron.*, vol. 9, no. 5, pp. 6196-6218, Oct. 2021.

[27] B. Zhang, J. Deng, L. Li, Z. Wang, S. Wang, and G. Guidi, "Thermal analysis and design of a 30kW EV wireless charger with liquid-cooled shell for magnetic coupler and integrated power converter," in *2021 IEEE Applied Power Electronics Conference and Exposition (APEC)*, Phoenix, AZ, USA, Jun. 2021, pp. 426–431.

[28] R. Bosshard, J. W. Kolar, J, "Fundamentals and multi-objective design of inductive power transfer systems," ETH, Nuremberg, Germany. May 19-21, 2015. [Online]. Available: https://www.pespublications.ee.ethz.ch/uploads/tx_ethpublications/PCIM_2015_IPT_Tutorial_RB_JWK_2_Version29aug2015.pdf.

[29] S. Bandyopadhyay, "Comparison of magnetic couplers for IPT-based EV charging using multi-objective optimization," *IEEE Trans. Veh. Technol.*, vol. 68, no. 6, pp. 5416-5429, Apr. 2019.

[30] New England wire, "Litz Design," New England Wire Technologies. Lisbon, New Hampshire, USA. [Online]. Available: http://www.litzwire.com/litz_design.htm.

[31] K. Peng and E. Santi, "Performance projection and scalable loss model of SiC MOSFETs and SiC Schottky diodes," in *2015 IEEE Electric Ship Technologies Symposium (ESTS)*, Old Town Alexandria, VA, USA, Jun. 2015, pp. 281–286.

[32] L. Meysenc, L. Saludjian, A. Bricard, S. Rael, and C. Schaeffer, "A high heat flux IGBT micro exchanger setup," *IEEE Trans. Comp. Hybrids Manuf. Tech* vol. 20, no. 3, pp. 334-341, 1997.

[33] J. E *et al.*, "Investigation on thermal performance and pressure loss of the fluid cold-plate used in thermal management system of the battery pack," *Appl. Therm. Eng.*, vol. 145, pp. 552–568, Dec. 2018.

[34] D. Copeland, "Optimization of parallel plate heatsinks for forced convection," in *Sixteenth Annual IEEE Semiconductor Thermal Measurement and Management Symposium (Cat. No.00CH37068)*, San Jose, CA, USA, 2000, pp. 266–272.

[35] X. Liu, D. Gerada, Z. Xu, M. Corfield, C. Gerada, and H. Yu, "Effective thermal conductivity calculation and measurement of Litz wire based on the porous metal materials structure," *IEEE Trans. Ind. Electron.*, vol. 67, no. 4, pp. 2667–2677, Apr. 2020.

2332-7782 (c) 2021 IEEE. Personal use is permitted, but republication/redistribution requires IEEE permission. See http://www.ieee.org/publications_standards/publications/rights/index.html for more information.
Authorized licensed use limited to: Sintef. Downloaded on May 20,2022 at 10:23:19 UTC from IEEE Xplore. Restrictions apply.

This article has been accepted for publication in a future issue of this journal, but has not been fully edited. Content may change prior to final publication. Citation information: DOI 10.1109/TTE.2022.3175806, IEEE Transactions on Transportation Electrification

[36] CelemSystem, "Guide to Using Celem Capacitors," Celem Power Capacitors, Jerusalem, Israel. May. 20, 2021. [Online]. Available: https://www.celem.com/guide_to_using_celem_capacitors.
[37] J. Deng, Y. Zhang, S. Wang, Z. Wang and Y. Yang, "The design and coupler optimization of a single-transmitter coupled multi-receiver inductive power transfer system for maglev trains," *IEEE Trans. Transp. Electrification*, vol. 7, no. 4, pp. 3173-3184, Dec. 2021.
[38] J. Biela and J. W. Kolar, "Cooling concepts for high power density magnetic devices," *IEEJ Trans. Ind. Appl.*, vol. 128, no. 4, pp. 500–507, 2008.
[39] X. Chen, S. Zeng, X. Liu, Y. Jin, X. Li, and X. Wang, "Design and realization of temperature measurement system based on optical fiber temperature sensor for wireless power transfer," in *the Fourth Seminar on Novel Optoelectronic Detection Technology and Application*, Nanjing, China, Feb. 2018, pp. 106972E1-E7.

Baokun Zhang received his B.S. degree in vehicle engineering from Beijing Institute of Technology, Beijing, China, in 2019. He is currently pursuing the Ph.D. degree in mechanical engineering with the National Engineering Laboratory for Electric Vehicles, at Beijing Institute of Technology. His research interests include the thermal design of inductive power transfer systems and bidirectional wireless power transfer.

JunJun Deng received his B.S., M.S. and Ph.D. degrees in electrical engineering from Northwestern Polytechnical University, Xi'an, China, in 2008, 2011 and 2015, respectively. From 2011 to 2014, he was a visiting scholar with the Department of Electrical and Computer Engineer, University of Michigan, Dearborn. In 2016, he joined the Faculty of Vehicle Engineering, Beijing Institute of Technology, Beijing, China. His research interests include wireless power transfer, resonant power conversion, and electric motor drive for electric vehicles.

Wenbo Wang was born in Jiangxi, China, in 1996. He received the B.S degree in automotive engineering from Hunan University, Hunan, China, in 2018. He is currently working toward the Ph.D. degree in mechanical engineering with the National Engineering Laboratory for Electric Vehicles, at Beijing Institute of Technology. His research interests include inductive power transfer and resonant converters.

Lantian Li received the B.S. degree in mechanical engineering from Beijing Institute of Technology, Beijing, China, in 2017. He is studying for a Ph.D. degree in mechanical engineering in the National Engineering Laboratory for Electric Vehicles from Beijing Institute of Technology, China and the Collaborative Innovation Center of Electric Vehicles in Beijing, China. His main research interests include the optimization of magnetic coupler and dynamic wireless power transfer.

Zhenpo Wang received the Ph.D. degree in automotive engineering from Beijing Institute of Technology, Beijing, China, in 2005. He is currently a Professor with Beijing Institute of Technology, the Associate Director of Collaborative Innovation Center for Electric Vehicles in Beijing and the Director of National Engineering Laboratory for Electric Vehicles. His current research interests include the pure electric vehicle integration, packaging and energy management of battery system and big data analysis. Prof. Zhenpo Wang has been the recipient of numerous awards including the Second Prize of National Science and Technology Progress.

Shuo Wang received the B.S. from Shandong University of Science and Technology, Qingdao, China, M.S. from China University of Mining and Technology, Beijing, China, and Ph.D. degree in engineering from the faculty of engineering and information technology (FEIT), University of Technology Sydney in 2017. He is Assistant Professor at Beijing Institute of Technology, Beijing. He was a Postdoctoral Research Fellow with the Beijing Institute of Technology (2017-2021). His research interests include wireless charging, electric vehicle and its big data analysis.

Giuseppe Guidi (M'00, SM'20) received the graduate degree from the University of L'Aquila, L'Aquila, Italy, in 1995, and the Ph.D. degree from the Norwegian University of Science and Technology (NTNU), Trondheim, Norway, in 2009. He has worked in the field of power electronics and industrial drives from 1997 to 2004, joining first Fuji Electric R&D, Japan, as R&D Engineer and then SIEI SpA, Italy, as a Senior Engineer. In 2009, he joined Yokohama National University, Yokohama, Japan, as a Research Associate, working on power converters for electric vehicles. From 2011 he was a part-time Research Associate with NTNU, until joining SINTEF Energy Research, Trondheim, Norway, in 2013. His current research interests include high power WPT systems for automotive and marine applications, drive systems for electric propulsion, as well as application of power electronics to renewable energy systems.

2332-7782 (c) 2021 IEEE. Personal use is permitted, but republication/redistribution requires IEEE permission. See http://www.ieee.org/publications_standards/publications/rights/index.html for more information.
Authorized licensed use limited to: Sintef. Downloaded on May 20,2022 at 10:23:19 UTC from IEEE Xplore. Restrictions apply.